Extensive MRO CRISM observations of 1.27 μm O2 airglow in Mars polar night and their comparison to MRO MCS temperature profiles and LMD GCM simulations

R. Todd Clancy, Brad J. Sandor, Michael J. Wolff, Michael D. Smith, Franck Lefèvre, Jean-Baptiste Madeleine, François Forget, Scott L. Murchie, Frank Seelos, Kim D. Seelos, et al.

Extensive MRO CRISM observations of 1.27 μm O_2 airglow in Mars polar night and their comparison to MRO MCS temperature profiles and LMD GCM simulations

R. Todd Clancy,[1] Brad J. Sandor,[1] Michael J. Wolff,[1] Michael D. Smith,[2] Franck Lefèvre,[3] Jean-Baptiste Madeleine,[4] Francois Forget,[4] Scott L. Murchie,[5] Frank P. Seelos,[5] Kim D. Seelos,[5] Hari A. Nair,[5] Anthony D. Toigo,[5] David Humm,[5] David M. Kass,[6] Armin Kleinböhl,[6] and Nicholas Heavens[6]

Received 27 October 2011; revised 22 May 2012; accepted 3 July 2012; published 22 August 2012.

[1] The Martian polar night distribution of 1.27 μm (0–0) band emission from O_2 singlet delta [$O_2(^1\Delta_g)$] is determined from an extensive set of Mars Reconnaissance Orbiter (MRO) Compact Reconnaissance Imaging Spectral Mapping (CRISM) limb scans observed over a wide range of Mars seasons, high latitudes, local times, and longitudes between 2009 and 2011. This polar nightglow reflects meridional transport and winter polar descent of atomic oxygen produced from CO_2 photodissociation. A distinct peak in 1.27 μm nightglow appears prominently over 70–90NS latitudes at 40–60 km altitudes, as retrieved for over 100 vertical profiles of $O_2(^1\Delta_g)$ 1.27 μm volume emission rates (VER). We also present the first detection of much ($\times 80 \pm 20$) weaker 1.58 μm (0–1) band emission from Mars $O_2(^1\Delta_g)$. Co-located polar night CRISM $O_2(^1\Delta_g)$ and Mars Climate Sounder (MCS) (McCleese et al., 2008) temperature profiles are compared to the same profiles as simulated by the Laboratoire de Météorologie Dynamique (LMD) general circulation/photochemical model (e.g., Lefèvre et al., 2004). Both standard and interactive aerosol LMD simulations (Madeleine et al., 2011a) underproduce CRISM $O_2(^1\Delta_g)$ total emission rates by 40%, due to inadequate transport of atomic oxygen to the winter polar emission regions. Incorporation of interactive cloud radiative forcing on the global circulation leads to distinct but insufficient improvements in modeled polar $O_2(^1\Delta_g)$ and temperatures. The observed and modeled anti-correlations between temperatures and 1.27 μm band VER reflect the temperature dependence of the rate coefficient for $O_2(^1\Delta_g)$ formation, as provided in Roble (1995).

Citation: Clancy, R. T., et al. (2012), Extensive MRO CRISM observations of 1.27 μm O_2 airglow in Mars polar night and their comparison to MRO MCS temperature profiles and LMD GCM simulations, *J. Geophys. Res.*, *117*, E00J10, doi:10.1029/2011JE004018.

1. Introduction

[2] The winter polar atmosphere of Mars exhibits distinctive compositional, thermal, and dynamical regimes that are poorly observed due to the lack of solar illumination, which leads to limited infrared and visible measurement opportunities. The polar winter (and late fall, early spring) atmosphere is separated from the global atmosphere by a polar vortex that limits lower level transport into and out-of the polar night region, as dramatically indicated by CO_2 condensation-related increases in polar night argon [*Sprague et al.*, 2007] and CO [*Smith et al.*, 2009] abundances. A substantial fraction of this atmospheric CO_2 conversion to surface CO_2 ice may occur through the formation of CO_2 snow clouds [*Colaprete and Toon*, 2002]. In any case, CO_2 clouds appear prevalent in the polar winter atmosphere [*Neumann et al.*, 2003; *Hayne et al.*, 2012], whereas dust and water ice aerosols have not been spectrally distinguished from such CO_2 clouds [*McCleese et al.*, 2010]. The implication of very pure CO_2 and water ice seasonal cap frosts [e.g., *Langevin et al.*, 2007] further points to extremely limited transport of water and dust into the winter polar lower atmosphere. At upper levels (above ~60 km) transport into the polar winter regions is less restricted, as predicted by models [e.g., *Haberle et al.*, 1993; *Forget et al.*, 1999] and evidenced by the presence of distinctive temperature

[1]Space Science Institute, Boulder, Colorado, USA.
[2]NASA Goddard Space Flight Center, Greenbelt, Maryland, USA.
[3]Laboratoire Atmosphères Milieux Observations Spatiales, Paris, France.
[4]Laboratoire do Météorologie Dynamique, Paris, France.
[5]Johns Hopkins University Applied Physics Laboratory, Columbia, Maryland, USA.
[6]Jet Propulsion Laboratory, Pasadena, California, USA.

Corresponding author: R. T. Clancy, Space Science Institute, 4750 Walnut St., Ste. 205, Boulder, CO 80301, USA. (clancy@spacescience.org)

0148-0227/12/2011JE004018

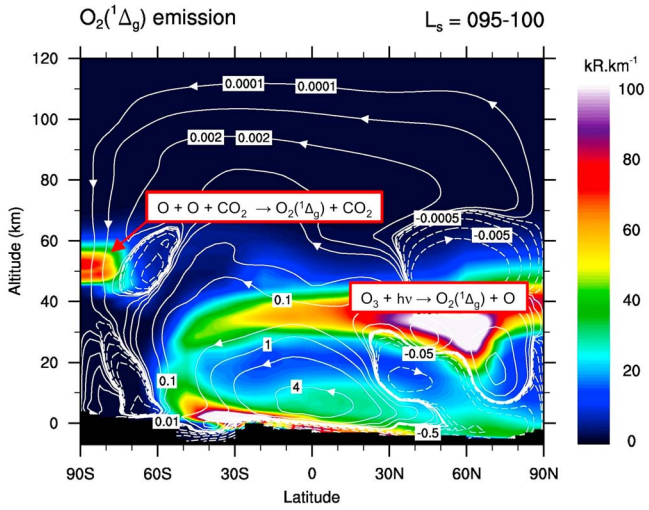

Figure 1. A schematic of the vertical and latitudinal distribution of Mars $O_2(^1\Delta_g)$ emission (kR/km, color contoured) for $L_S = 95–100°$ as simulated by the LMD GCM. The meridional stream function (10^9 kg/s) is superimposed in white contour lines. Two primary pathways for $O_2(^1\Delta_g)$ production are the photolysis of ozone over solar illuminated latitudes (60S-90N) below 40 km, and the three body recombination of atomic oxygen over (mostly) unilluminated fall-winter-spring polar latitudes above 40 km altitudes.

increases associated with the downwelling branch of the winter hemisphere Hadley circulation [*Conrath et al.*, 1973; *Smith et al.*, 2001; *McCleese et al.*, 2008]. This downwelling is also characterized by poleward transport of dayside photolysis products and subsequent polar nightglow associated with their recombination, first evidenced by Mars Express (MEX) observations of nitric oxide (NO) ultraviolet airglow in southern polar winter night [*Bertaux et al.*, 2005].

[3] Two recent sets of limb profile measurements from the MEX OMEGA and SPICAM experiments [*Bertaux et al.*, 2012; *Montmessin et al.*, 2011] and the current MRO CRISM investigation further indicate chemical transport associated with this same upper atmospheric circulation. These measurements reflect the meridional transport of atomic oxygen, produced at lower sunlit latitudes, into the winter upper atmosphere (altitudes above 80–100 km). Entrained in the descending branch of this strong upper level Hadley circulation, upper level (enhanced) atomic oxygen abundances are transported downward over polar latitudes to higher pressure levels where three-body reactions,

$$O + O + CO_2 \rightarrow O_2(^1\Delta_g) + CO_2 \quad (1)$$

$$O + O_2 + CO_2 \rightarrow O_3 + CO_2 \quad (2)$$

produce $O_2(^1\Delta_g)$ and O_3 (Figure 1). These polar night, high altitude (40–70 km) layers of $O_2(^1\Delta_g)$ and O_3 are very distinct in origin and occurrence from Mars lower level $O_2(^1\Delta_g)$ and O_3 abundances, which are associated with local photolysis of O_3 and CO_2, respectively [e.g., *Noxon et al.*, 1976; *Nair et al.*, 1994]. Figure 1 schematically distinguishes these two regimes of $O_2(^1\Delta_g)$ emission in the Mars atmosphere, including their distinct spatial distributions. The upper level, winter polar $O_2(^1\Delta_g)$ and O_3 behaviors are in fact more closely related to the production of $O_2(^1\Delta_g)$ in the nightside lower thermosphere of Venus [e.g., *Crisp et al.*, 1996]. The transport related origin of these Mars polar night oxygen species provides for a unique window into the upper level circulation of the Mars atmosphere. The CRISM $O_2(^1\Delta_g)$ observations in particular support extensive spatial and seasonal comparisons to general circulation model (GCM) simulations of this transport.

[4] In the following, we present the extended set of CRISM $O_2(^1\Delta_g)$ measurements obtained in Mars polar night at northern and southern high latitudes. These limb profile measurements sample a wide range of Mars latitudes, longitudes, and local times; as accumulated from a set of dedicated CRISM limb observations taken at solar longitudes (L_S) of 51°, 64°, 75°, 95°, 134°, 165°, 195°, 265°, and 295° over the July 2009 - May 2011 period (Table 1). Inversion of the CRISM limb radiances for vertical profiles of volume emission rate (VER) yields the detailed spatial and seasonal distribution of Mars $O_2(^1\Delta_g)$ polar nightglow, which is compared to model simulations generated by the Laboratoire de Météorologie Dynamique (LMD) GCM with photochemistry [*Lefèvre et al.*, 2004, 2008]. Recent modifications to this code [*Madeleine et al.*, 2011a] are considered in the context of these model-data comparisons for Mars polar $O_2(^1\Delta_g)$ nightglow, as well as contemporaneous/co-located temperature profile measurements obtained from the MRO Mars Climate Sounder (MCS) [*McCleese et al.*, 2008]. In particular, the radiative influence of clouds are shown to significantly impact winter polar $O_2(^1\Delta_g)$ and temperature distributions. We also report CRISM limb detection of weak 1.58 μm band emission associated with Mars polar $O_2(^1\Delta_g)$ nightglow.

2. CRISM Limb Imaging $O_2(^1\Delta_g)$ Observations

[5] The MRO CRISM instrument is an imaging spectrometer, designed to obtain moderate spectral (7–15 nm), high spatial resolution (15–20 m/pixel) surface spectra for Mars over the 0.4–3.9 μm visible/near-infrared spectral region [*Murchie et al.*, 2007]. Although the primary CRISM science objectives regard surface compositional variations at high spatial resolution, a significant number of atmospheric

Table 1. CRISM Limb $O_2(^1\Delta_g)$ Nightglow Observation Summary

Date[a]	Year[b]	MY[c]	L_S[d]	Pole[e]	Profiles[f]	$O_2(^1\Delta_g)$, T[g]
July 10–11	2009	29	301°	N	4	$O_2(^1\Delta_g)$ only
February 10–11	2010	30	50°	S	9	$O_2(^1\Delta_g)$, T
April 7	2010	30	74°	S	11	$O_2(^1\Delta_g)$, T
April 28–29	2010	30	84°	S	11	$O_2(^1\Delta_g)$, T
May 26	2010	30	96°	S	12	$O_2(^1\Delta_g)$, T
August 22–23	2010	30	137°	S	23	$O_2(^1\Delta_g)$, T
October 17	2010	30	166°	N,S	12	$O_2(^1\Delta_g)$ only
December 5–6	2010	30	193°	N,S	14	$O_2(^1\Delta_g)$ only
March 31–April 1	2011	30	265°	N	4	$O_2(^1\Delta_g)$ only
May 14–15	2011	30	293°	N	4	$O_2(^1\Delta_g)$ only

[a]UT month, day of CRISM (MCS) observations.
[b]UT year of CRISM (MCS) observations.
[c]Mars Year of CRISM (MCS) observations, as in *Clancy et al.* [2000].
[d]Solar longitude of CRISM (MCS) observations.
[e]Polar region observed.
[f]Number of CRISM limb profile retrievals for $O_2(^1\Delta_g)$ nightglow.
[g]Co-located MCS temperature profiles compared for SP winter periods.

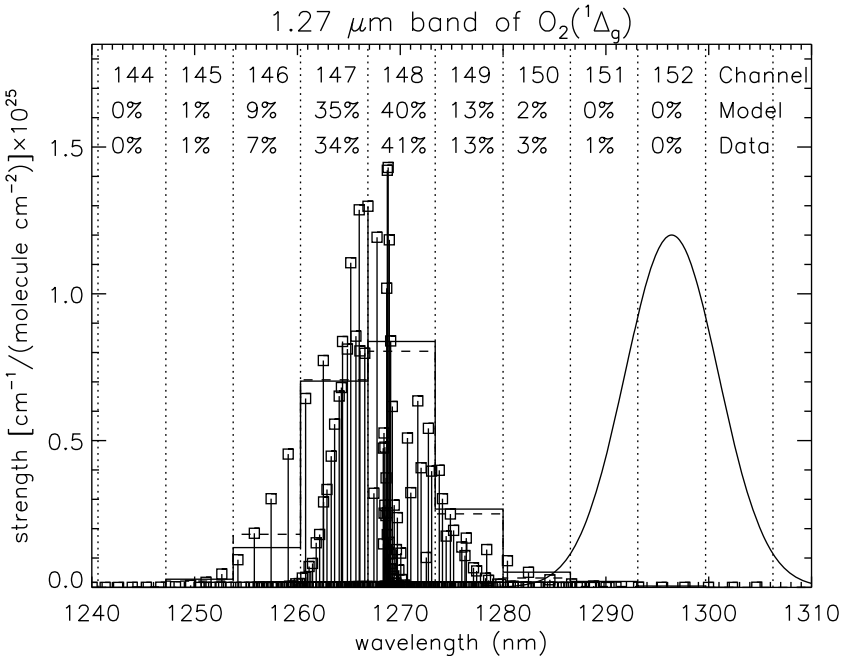

Figure 2. The grand average (see Figure 4) CRISM limb spectrum of polar night $O_2(^1\Delta_g)$ 1.27 μm limb emission (solid histogram line) is compared against the predicted 1.27 μm lineshape (dashed histogram line) based upon; the CRISM channel spacing/locations (dotted vertical lines), the CRISM instrumental resolution (solid Gaussian line at right, FWHM = 10.7 nm), and the location and relative strength of $O_2(^1\Delta_g)$ emission lines from 2008 HITRAN (vertical lines and box symbols, scale of vertical axis). At the top of the figure, CRISM channel numbers and the percentage of integrated 1.27 μm emission contained in each CRISM channel, based on the observed spectrum (data) and the calculated spectrum (model), are provided.

spectral features are incorporated in the CRISM spectral range including multiple band absorptions for CO_2 (1.4, 2.0, 2.7 μm), H_2O (1.35, 1.9, 2.6 μm), and CO (2.35 μm). Column retrievals for Mars atmospheric water and carbon monoxide have been mapped versus latitude and season on the basis of these atmospheric band absorptions [*Smith et al.*, 2009]. CRISM aerosol analyses have also been conducted based upon broad-band absorptions associated with silicate and ice particulate compositions [*Wolff et al.*, 2009; M. D. Smith et al., Vertical distribution of dust and water ice aerosols from CRISM limb-geometry observations, submitted to *Journal of Geophysical Research*, 2012]. With respect to this current CRISM analysis, O_2 band emission at 1.27 μm is present in CRISM spectra, similar in nadir signal characteristics to that reported from MEX OMEGA spectral imaging observations by *Altieri et al.* [2009]. That is to say, the coarse spectral resolution of CRISM does not reveal the band structure of $O_2(^1\Delta_g)$ emission, but simply captures the integrated emission. Figure 2 indicates the CRISM channel widths against the band structure of the 1.27 μm emission from the electronically excited, singlet delta state of molecular oxygen, $O_2(^1\Delta_g)$.

$$O_2(^1\Delta_g) \rightarrow O_2(X^3\Sigma_g, \nu'' = 0) + h\nu; \lambda = 1.27\,\mu\text{m}. \quad (3)$$

[6] The (unresolved) band structure is indicated by the distribution and relative strengths of the individual rotational lines, from the 2008 HITRAN data base (vertical lines topped by squares, [*Rothman et al.*, 2009]). CRISM spectral channels are indicated by dotted vertical lines channel numbers are indicated along the top of Figure 2. The instrumental spectral resolution is roughly twice these channel widths, as indicated by the Gaussian solid line to the right of the band emission (FWHM $\sim$ 10.7 nm). The solid histogram spectrum presents the observed spectral profile of 1.27 μm $O_2(^1\Delta_g)$ emission, based upon an extensive average of CRISM limb observations, as discussed subsequently. The dashed histogram spectrum presents the modeled spectral profile of 1.27 μm $O_2(^1\Delta_g)$ emission, based upon HITRAN data and the CRISM spectral parameters. The percentage of integrated 1.27 μm band emission sampled within each CRISM channel, based upon the observed spectra, is provided across the top of Figure 2, labeled Data. The percentage of integrated 1.27 μm band emission sampled within each CRISM channel, based upon the modeled spectral weighting, is also provided across the top of Figure 2, labeled Model. The minor disagreement between the modeled and observed spectral shapes lies well within the uncertainty of the CRISM spectral resolution (*i.e.*, 10.7 nm) at this wavelength.

[7] The primary focus of CRISM $O_2(^1\Delta_g)$ limb observations is dayside vertical profiling in support of atmospheric photochemistry studies. Indeed, CRISM limb observations of $O_2(^1\Delta_g)$ dayglow constitute a unique atmospheric measurement relevant to Mars ozone photochemistry and $O_2(^1\Delta_g)$ collisional de-excitation rates in a CO_2 atmosphere. Strong seasonal and latitudinal variations in the intensity and vertical

distribution of $O_2(^1\Delta_g)$ dayglow are presented in the 2009–2011 CRISM limb spectra, indicating distinct orbital and seasonal variations associated with atmospheric water vapor distribution [*Clancy and Nair*, 1996; *Lefèvre et al.*, 2004] and perhaps heterogeneous chemistry on water ice clouds [*Lefèvre et al.*, 2008]. Retrievals for dayside profiles of $O_2(^1\Delta_g)$ emission will be provided in following analyses in support of such photochemical investigations. However, the current analysis focuses on $O_2(^1\Delta_g)$ emission observed at high altitudes over fall-winter-spring conditions of polar night. This emission presents a new window in the investigation of atmospheric circulation. It also presents a less difficult profile retrieval problem relative to dayside $O_2(^1\Delta_g)$ radiative transfer (RT), and so constitutes our initial presentation of CRISM profile retrievals for Mars $O_2(^1\Delta_g)$ emission. These retrievals for band integrated $O_2(^1\Delta_g)$ polar nightglow from CRISM limb imaging observations are developed in the following section. Here, we indicate the frequency and spatial characteristics of the CRISM limb observations pertinent to measurement of Mars $O_2(^1\Delta_g)$ dayglow and polar nightglow.

[8] Dedicated CRISM limb observations began in July of 2009, with the goal of retrieving vertical profiles for Mars atmospheric water vapor, CO, $O_2(^1\Delta_g)$, and dust/ice aerosols as a function of Mars season and latitude. The CRISM pointing gimbal does not provide sufficient scan motion for limb access, such that it is necessary to perform MRO spacecraft yaw maneuvers to place the CRISM field-of-view (fov) at the atmospheric limb, in the plane of the MRO orbit. In addition, the CRISM detector coolers have degraded considerably since 2009 to the degree that CRISM limb observations constitute a significant requirement on cooler operations. Consequently, CRISM limb observations are operationally intensive from both mission and experiment perspectives. They also, with the exception of MCS observations, preclude observations from other MRO investigations. In these lights, CRISM limb operations are limited to two full orbits roughly every two months (or 30° intervals of L_S). This provides pole-to-pole coverage at 6–12° intervals of latitude, for two separated Mars longitudes of ~105W and 300W (at the equator, corresponding to Tharsis ridge and Hellas basin longitudes). Due to spacecraft safing, conjunction, and other operational considerations, the actual frequency of CRISM limb observations has deviated significantly from the baseline two month cycle. There was also an attempt to provide global limb coverage (equivalent to one full day of MRO orbits) in August of 23–24, 2010. However, the CRISM detector coolers were not able to maintain sufficiently cold detector temperatures for a large fraction of those orbits. Table 1 indicates the full set of 2009–2011 limb orbit observations for which $O_2(^1\Delta_g)$ polar nightglow is analyzed here.

[9] CRISM limb observations are performed with the spatial dimension of the visible/near-infrared detector arrays aligned parallel to the atmospheric horizon. The atmospheric limb is scanned in-track with the CRISM gimbal, from limb tangents below the surface to altitudes above 120 km. The polar $O_2(^1\Delta_g)$ nightglow is observed to be present only over 40–70 km limb tangent altitudes. The nominal limb resolution is of order 50 meters, however the CRISM spectral data are 10× binned horizontally (in detector pixels) and vertically (in image summing) to reduce data rates. This leads to vertical intervals of ~500 meters for which 64 spectra are returned along the north or south oriented limbs (depending on the location of the Sun). We further average the central 40 of these spectra to obtain a single limb profile of visible-near-infrared radiances, in order to obtain maximum signal-to-noise ratios. Variations along the ~30 km limb horizon are unlikely to yield useful spatial information, given the in-orbit ~300 km limb tangent paths.

3. Limb Profile Retrievals for $O_2(^1\Delta_g)$ Volume Emission Rates

[10] As indicated in Figure 2, CRISM spectra are appropriate to measuring the integrated $O_2(^1\Delta_g)$ band emission at 1.27 μm. CRISM nightglow limb analysis is distinct in several respects to the dayglow, nadir analyses of *Altieri et al.* [2009] and *Fedorova et al.* [2006] regarding MEX OMEGA and SPICAM $O_2(^1\Delta_g)$ observations, respectively. Obviously, vertical profile retrievals for $O_2(^1\Delta_g)$ emission are supported by limb radiance observations. Spectrally dependent absorption and scattering contaminations that require detailed corrections for nadir dayside spectra may be safely neglected in the analysis of these nightglow observations. Furthermore, limb path extinction of the $O_2(^1\Delta_g)$ nightglow by suspended dust and ice aerosols proves unimportant in the aerosol-free (above 20–30 km) polar winter atmosphere. Three such Mars polar nightglow measurements were obtained from MEX OMEGA limb observations, the analyses of which are presented in *Bertaux et al.* [2012]. Here we discuss the spectral, radiative transfer, and profile retrieval aspects of inverting a much larger set of CRISM limb observations of $O_2(^1\Delta_g)$ polar nightglow for vertical profiles of 1.27 μm volume emission rates (VER). We also demonstrate the basic characters of CRISM limb radiance profiles and spectra for polar night $O_2(^1\Delta_g)$ 1.27 μm band emission, as well as the first detection of Mars $O_2(^1\Delta_g)$ 1.58 μm band emission.

3.1. Polar Night $O_2(^1\Delta_g)$ Limb Spectra for 1.27 μm and 1.58 μm Band Emission

[11] Figure 3 presents a moderately bright spectrum of Mars $O_2(^1\Delta_g)$ polar nightglow as observed in April of 2010 (L_S = 74°), at a limb tangent altitude of 50 km near 80S latitude. The winter polar night presents negligible limb path extinction at these altitudes associated with aerosols, as indicated by coincident MCS limb profile measurements. Radiance units are presented as reflectance (0.001 × I/F) in this case to demonstrate the level of the band emission relative to surface spectral reflectances CRISM is designed to observe (*e.g.*, 0.002 versus 0.2). The $O_2(^1\Delta_g)$ band emission signal stands well above the spectral noise in the dark-count subtracted background of these nightside limb views. Detector/filter boundaries appear as spikes near 1.0, 1.65, and 2.7 μm wavelengths and thermal noise increases rapidly beyond 2.7 μm, as described in *Murchie et al.* [2007]. Figure 4 presents a grand average of over 1000 such CRISM limb radiance spectra for the 1.1–1.8 μm spectral window (Figure 4, top). This average limb spectrum incorporates all limb spectra observed over the 46–55 km limb tangent (aeroid) altitude range, for February 2010- May 2011 polar night limb observations in which 1.27 μm polar nightglow is detected. In this presentation, the CRISM spectrum is provided in modified absolute radiance units (mW/

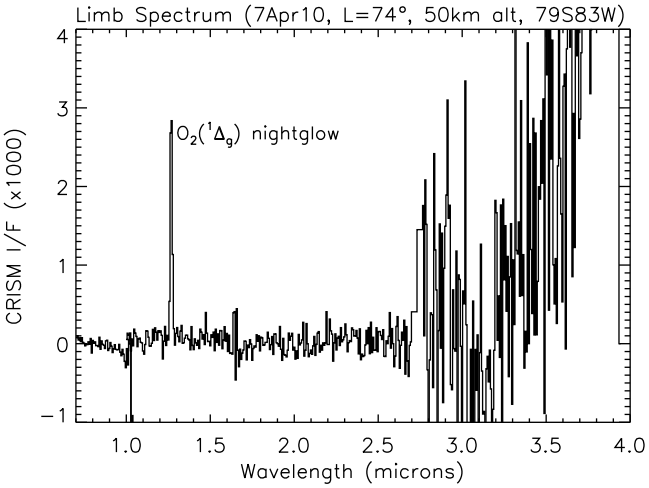

Figure 3. The CRISM visible/near-IR spectrum of polar night limb radiance (in I/F x 1000 units) for a limb tangent altitude of 50 km (aeroid height) at 79S, 83W on April 7, 2010 (L_S = 74°). The 1.27 μm emission line of $O_2(^1\Delta_g)$ appears prominently above the background level, which presents discontinuities at detector/filter boundaries and increased noise/background levels beyond 2.7 μm wavelengths [*Murchie et al.*, 2007].

[$m^2 \cdot \mu m \cdot$steradians], or 1/1000 of standard CRISM radiance values). This grand average indicates that the majority of the 1.27 μm $O_2(^1\Delta_g)$ band emission is contained in four CRISM channels centered at 1.27 μm. The expanded scale presented in Figure 4 (bottom) indicates a 3σ detection of extremely weak 1.58 μm band emission from $O_2(^1\Delta_g)$, the first detection of this emission in the Mars atmosphere. The predicted ratio for 1.27 μm/1.58 μm band emission (based upon molecular theory and laboratory measurements) is somewhat uncertain, but has been observed in the Venus nightside lower thermosphere with a ratio of 78 $\pm$ 10 [*Piccioni et al.*, 2009]. The observed Mars band ratio is 80 $\pm$ 20, where the large uncertainty is significantly impacted by uncertainty in the spectral baseline. This $O_2(^1\Delta_g)$ band radiance ratio is in agreement with but considerably more uncertain than that determined for Venus (where peak $O_2(^1\Delta_g)$ emission rates are 5–10 times greater). This result is primarily a testament to the dynamic range of CRISM spectral sensitivity with respect to nightglow detection (*i.e.*, in the absence of a scattered light continuum level).

3.2. Polar Night $O_2(^1\Delta_g)$ Limb Emission Profiles

[12] CRISM limb profiles of $O_2(^1\Delta_g)$ band emission are calculated as the difference between a two channel sum centered at 1.267 μm (channel numbers 147,148 in Figure 2) and the sum of bounding channels centered at 1.257 and 1.283 μm (channel numbers 146 and 150). This minimizes spectral noise in the retrieved band emission and provides optimum subtraction of spectral background radiance associated with issues such as incomplete dark count subtraction. Analysis of the CRISM limb average spectrum indicates that the central two channel sum incorporates 75% of the integrated 1.27 μm band emission, versus 10% of the band emission contained in the two bounding channels (see Figure 2), such that the channel difference effectively determines 65% of the total 1.27 μm $O_2(^1\Delta_g)$ band emission. By comparison, the predicted proportion of integrated 1.27 μm band emission for this channel difference is 64%, based upon the CRISM spectral resolution (FWHM of 10.7 nm), channel wavelengths, and 1.27 μm band structure as calculated for an atmospheric temperature of 160 K (also Figure 2). For band emission calibrations, we adopt the observed 65% proportion determined from the average CRISM limb spectrum of 1.27 μm band emission (Figures 1 and 3) and estimate a 2% uncertainty in this calibration factor. This uncertainty is also roughly equivalent to the effects of a $\pm$20 K perturbation to atmospheric temperature on the $O_2(^1\Delta_g)$ band structure.

[13] Such calibrated 1.27 μm emission profiles are constructed for all CRISM polar night limb observations. For the purposes of the current analysis, polar night regions are defined by latitudes poleward of 70NS during fall-winter-spring seasons. Figure 5 presents a set of four such 1.27 μm limb radiance profiles, indicating both peak intensity and limb tangent altitude variations. In all presented profiles, the altitude scale is calculated with respect to the Mars aeroid surface. The limb radiance units for Figure 5 are (Mega) Rayleighs, a standard unit of airglow line emission ($4\pi \times$ brightness units of 10^6 photons/[cm^2/second/sterad] [*Hunten et al.*, 1956]). These units correspond to previous ground-based [e.g., *Novak et al.*, 2002; *Krasnopolsky*, 2003] and spacecraft-based [*Fedorova et al.*, 2006; *Altieri et al.*, 2009] presentations of Mars 1.27 μm band emission. They also support equivalent comparisons to model 1.27 μm volume

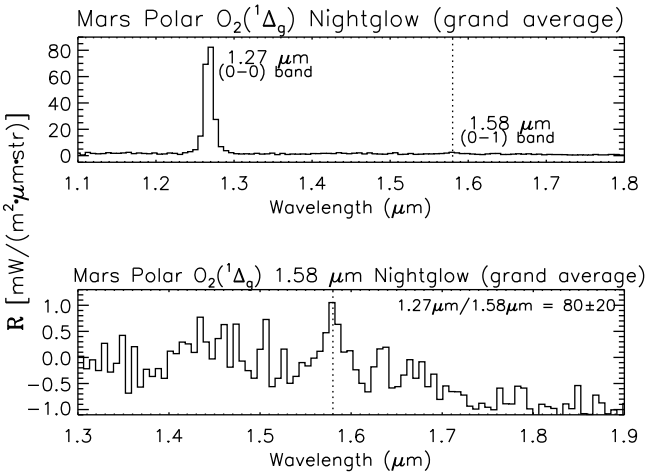

Figure 4. (top) A grand average of all CRISM polar night limb spectra containing substantial 1.27 μm emission over 2010–2011 and at limb tangent altitudes between 46 and 55 km is presented for the 1.1 to 1.9 μm spectral region. Standard CRISM radiance units ($\times$1000, *i.e.* mW) are employed. The 1.27 μm line emission of $O_2(^1\Delta_g)$ is well characterized in this average, whereas very weak 1.58 μm emission is less apparent. (bottom) Expansion of the 1.3–1.9 μm spectral region to illuminate the first detection of this weak 1.58 μm emission in the Mars atmosphere. The 1σ absolute uncertainty in Y-axis radiance is 5% (see text).

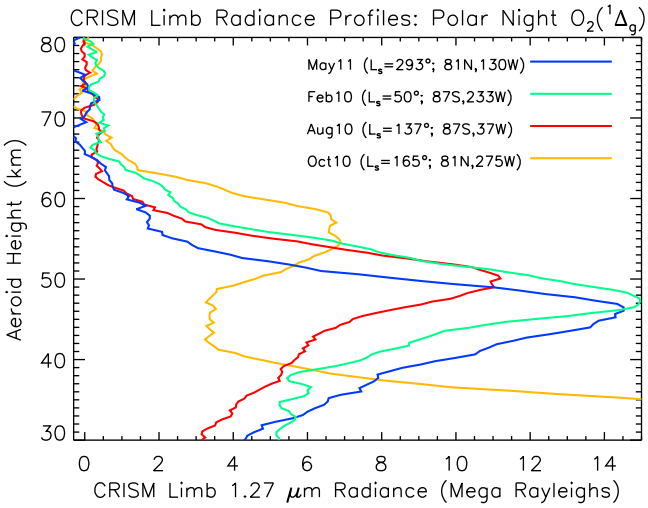

Figure 5. Four CRISM $O_2(^1\Delta_g)$ 1.27 μm limb radiance profiles are plotted versus limb tangent aeroid height. These limb radiances are presented in units of Mega Rayleighs (see text), as calibrated for the total band emission and CRISM spectral characteristics. Significant seasonal variation in the amplitude and peak altitude of limb emission is indicated among the set of high latitude (81–87°) NP (L_S = 165, 293°) and SP (L_S = 50, 137°) observations. The portion of the L_S = 165° profile below 40 km exhibits $O_2(^1\Delta_g)$ associated with low solar elevation photolysis of ozone.

emission rates (in units of kilo Rayleighs/km). Four periods of CRISM limb observations are represented in Figure 5, spanning a range of Mars seasons at northern and southern high latitudes. Significant spatial (latitude and longitude) and local time (LT) variations also occur within each season/observing period, as demonstrated in Figure 6. In this case, all CRISM limb observations obtained over 70S-90S latitudes among CRISM limb observations on April 7, April 28, and May 28 (L_S = 74–96°) are distinguished by latitude bins of 70S–80S (dashed lines) and 80S-90S (solid lines). CRISM polar limb observations extend over the South pole (but not the North pole, as yet) to obtain both AM and PM local times (LT) of observation. As discussed in following model-data comparisons, the apparent larger variability of $O_2(^1\Delta_g)$ emission over 70S-80S versus 80S-90S latitude bands primarily reflects larger diurnal rather than spatial variation at lower latitudes. In addition, all observed periods exhibit significant (10's of %) increases in average (over LT and longitude) $O_2(^1\Delta_g)$ nightglow emission toward higher latitudes.

3.3. Limb to Profile Matrix Inversion

[14] The derivation of $O_2(^1\Delta_g)$ volume emission rates (VER) from CRISM limb profiles of 1.27 μm radiance requires geometric inversion from vertical profiles of integrated limb path emission to vertical profiles of per unit volume emission. Given emission noise levels and the narrow vertical region of $O_2(^1\Delta_g)$ emission, we have adopted a non-linear matrix inversion technique constrained to yield positive-only solution values [*Clancy et al.*, 1982]. The radiative transfer (RT) of 1.27 μm limb emission is obligingly simple in the Mars polar night regions, due to negligible scattering associated with zero or minimal solar illumination coupled with the absence of significant molecular or aerosol opacities at the 40–60 km altitudes of polar 1.27 μm nightglow. Upper limits for aerosol extinction in the polar night are provided by coincident Mars Climate Sounder (MCS) limb profiling, albeit at thermal infrared wavelengths. Nevertheless, minimal 1.27 μm aerosol extinction along the limb path of $O_2(^1\Delta_g)$ emission is indicated for currently measured Mars aerosol particle sizes (R_{eff} of 1–3 μm). For conditions of high incident angle solar illumination (October and December 2010 observations), visible and near-infrared portions of the CRISM spectral limb radiances indicate negligible aerosol opacities at 40–60 km altitudes. Self-absorption is also negligible (limb path $\tau < 10^{-4}$) due to the very low O_2 abundances. Consequently, the simplest of limb RT conditions are assumed, in which the $O_2(^1\Delta_g)$ radiance is approximated by a vertical profile of $O_2(^1\Delta_g)$ 1.27 μm VER integrated along a limb path geometry. The inversion weighting matrix, P(i, j), is constructed as simple limb path weights to the VER profile, E(j). The linear matrix equation becomes:

$$\sum_{j=1,nl} P(i,j)\cdot E(j) = S(i), \tag{4}$$

where S(i) are the limb radiance observations and the summation is conducted from layer 1 to the top layer of solution, nl. However, P(i, j) values below a given tangent layer, i, of observation (*i.e.*, j = 1 to i-1) are zero. In order to specify non-negative solution E(j), or VER, we construct a non-linear matrix equation in which the solution vector E(j) is expressed as $e^{X(j)}$ and the matrix equation becomes:

$$\sum_{j=1,nl} P(i,j)\cdot e^{X(j)} = S(i). \tag{5}$$

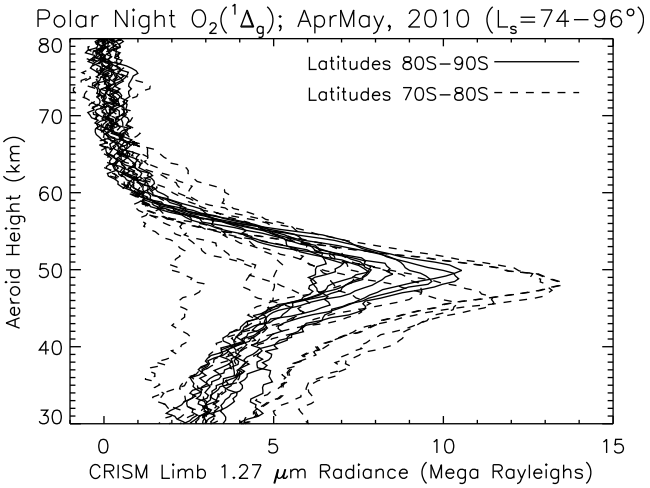

Figure 6. CRISM limb radiance profiles of 1.27 μm $O_2(^1\Delta_g)$ emission, as in Figure 5, from SP winter limb observations obtained in April and May of 2010 (L_S = 74–96°). Latitude bands of 70-80S and 80-90S are distinguished as dashed and solid lines, respectively. The much greater variability apparent at 70-80S latitudes primarily reflects LT (diurnal) rather than spatial variation.

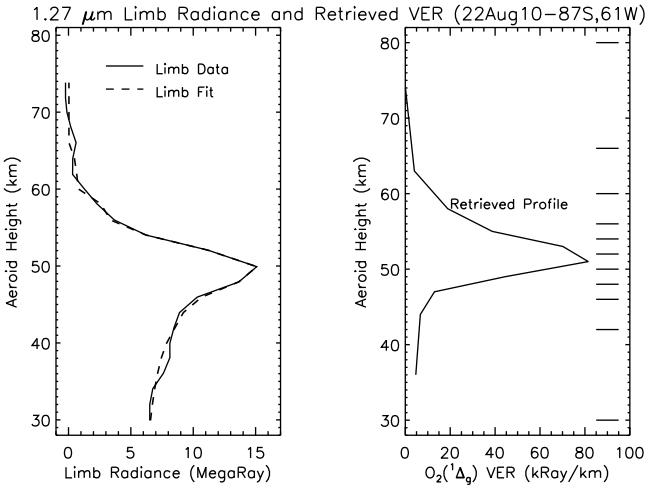

Figure 7. A non-linear matrix inversion is adopted to invert CRISM limb radiance profiles of (left) integrated $O_2(^1\Delta_g)$ 1.27 μm band emission to (right) vertical profiles of 1.27 μm volume emission rates (VER in kilo Rayleighs/km). The solid line in Figure 7, left, compares the observed 1.27 μm band emission for an August 2010 limb observation (L_S = 137°) against the RT model limb radiance profile (dashed line) associated with the retrieved 1.27 μm VER (solid line in Figure 7, right). The solution retrieved VER profile is specified for discrete vertical layers indicated by horizontal lines at the right side of Figure 7, right.

The partial differential matrix, PD(i, j), for X(j) iterative solution is simply:

$$PD(i,j) = P(i,j)\cdot E(j). \quad (6)$$

[15] We have experimented with a variety of layer thicknesses and numbers. Minimum layer thicknesses of 2 km are chosen for the primary altitude region of $O_2(^1\Delta_g)$ nightglow between 46 and 56 km. Increasingly broader layers are employed for solution over the lower boundary 30–46 km and upper boundary 56–80 km regions. A total of 10 layers are determined for the full 30–80 km range of solution. Solutions for 12 layers lead to negligible changes in derived VER over the altitude region of significant $O_2(^1\Delta_g)$ nightglow.

[16] Figure 7 presents the observed (solid line) and fitted (dashed line) limb radiance profiles (Figure 7, left), and the retrieved VER profile (Figure 7, right) for a CRISM limb observation obtained in August 22 of 2010 (L_S = 137°). The retrieval algorithm adopts an initialized, uniform VER profile (equivalent to ~15 kRay/km), and quickly converges to solution VER profiles that provide accurate fits to all observed nightglow limb radiance profiles. The solution layers, indicated by horizontal bars on Figure 7 (right, right side), provide adequate representation of the VER 1.27 μm nightglow profile of VER within the uncertainties of the limb radiance observations. Figure 8 presents $O_2(^1\Delta_g)$ VER profile retrievals associated with the four limb radiance profiles presented in Figure 5.

[17] The uncertainties in retrieved $O_2(^1\Delta_g)$ VER for these polar night conditions (where aerosol extinction is negligible) include contributions from absolute (constant scaling for all profiles) and measurement noise (per individual retrieved profile) error sources. The absolute 1σ uncertainty is 5%, as dominated by the radiometric calibration error for CRISM radiances in the 1.27 μm wavelength region [*Murchie et al.*, 2009; D. Humm, personal communication, 2011]. This includes the small (2%) uncertainty associated with calculation of integrated $O_2(^1\Delta_g)$ band intensity from the individual CRISM channel differences. The noise-limited uncertainty for individual retrieved $O_2(^1\Delta_g)$ VER is 4 kR/km, as determined from the binned (vertically and horizontally) noise level of the CRISM limb radiances and the covariance matrix associated with vertical profile retrievals.

4. $O_2(^1\Delta_g)$ Volume Emission Rate (VER) Profiles

[18] As a measure of our current understanding of chemistry and dynamics within the polar middle atmosphere, we present the full set of retrieved CRISM $O_2(^1\Delta_g)$ VER profiles in the context of LMD GCM VER profiles and coincident MCS temperature measurements. The characteristics of winter polar temperature and $O_2(^1\Delta_g)$ nightglow profiles are determined in large part by upper level (50–100 km) circulation into the Mars polar regions. This circulation is globally forced in association with spatially and temporally varying distributions of solar heating and thermal cooling. Polar winter dynamics is particularly dependent on "distant" circulation at low latitudes, as well as upper level boundary conditions. As a consequence, the observed behavior of polar $O_2(^1\Delta_g)$ nightglow can only be understood in the context of the global Mars circulation. We begin with short descriptions of the comparison LMD GCM $O_2(^1\Delta_g)$ simulations and MCS temperature profiles.

4.1. LMD GCM Photochemical Modeling

[19] The CRISM $O_2(^1\Delta_g)$ and MCS temperature profiles are compared to those calculated by the LMD GCM with interactive photochemistry [*Lefèvre et al.*, 2004, 2008]. In the configuration used here, the model is integrated on 35 levels extending from the surface up to about 150 km,

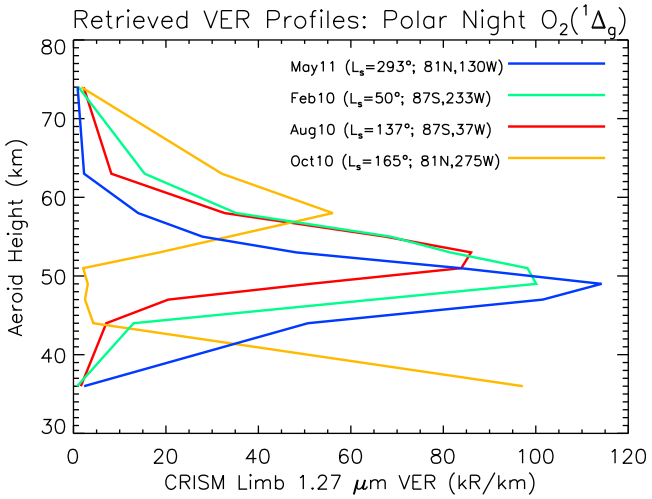

Figure 8. Vertical profiles of retrieved $O_2(^1\Delta_g)$ 1.27 μm VER are presented for the four CRISM limb radiance observations presented in Figure 5.

and the horizontal resolution is 3.75° latitude × 5.6° longitude. The photochemical package computes the evolution of 16 chemical species as well as the $O_2(^1\Delta_g)$ emission produced either by ozone photolysis or by the termolecular association of O atoms in reaction (1). For this latter process, a net effective yield of 0.75 is adopted for the production of $O_2(^1\Delta_g)$. This value proposed by *Crisp et al.* [1996] is in good agreement with the value of 0.7 recently derived for Mars and Venus by *Krasnopolsky* [2010a, 2011]. Both studies used a comprehensive scheme of the transfer of excitation from the seven electronic states of O_2 produced in reaction (1). Therefore, the production of $O_2(^1\Delta_g)$ calculated by the LMD GCM does take into account the cascade of energy and the production of $O_2(^1\Delta_g)$ from the higher electronic states of O_2.

[20] The expression used for the rate coefficient of reaction (1) is taken from *Roble* [1995]:

$$k1(T) = 9.46 \times 10^{-34} \exp(480/T). \quad (7)$$

[21] This exponential law is essentially constrained by the laboratory measurements of *Campbell and Gray* [1973] performed at 298 K and 196 K. It predicts a reaction rate which is ~20% slower but within the domain of uncertainty of the recent measurement of k1 carried out at 171 K by *Smith and Robertson* [2008]. The strong increase of k1 with decreasing temperatures is not fully understood from a theoretical point of view, and there are no laboratory data available in the domain of T < 170 K explored during the Mars polar night. In addition, experimental measurements of k1 are performed in a bath of N_2, which is recognized to be a less efficient third body than CO_2. To account for this effect, k1 and all three-body reactions are multiplied by a factor of 2.5 in the LMD model. This value has often been adopted in the modeling community since the proposition of *Nair et al.* [1994] but has not been precisely determined for reaction (1). In summary, due to the lack of laboratory data relevant to the Mars atmosphere, the value of k1 used in the LMD model simulations (and in all other models) is subject to a large uncertainty, especially at low temperatures.

[22] Once produced by reaction (1), $O_2(^1\Delta_g)$ emits a photon at 1.27 μm by radiative decay with a characteristic lifetime τ, or is quenched by collision with CO_2. In the LMD model, τ is equal to 4460 s from the measurements of *Lafferty et al.* [1998], whereas the quenching rate is 10^{-20} cm^3 s^{-1} [*Krasnopolsky*, 2010b]. At the altitudes considered in our study (z > 40 km) the slow quenching rate of $O_2(^1\Delta_g)$ by CO_2 plays a negligible role and is not a source of uncertainty.

[23] Two versions of the LMD GCM are used for the comparison. The first version, referred to as the "*standard*" version, is that described in *Lefèvre et al.* [2004]. The so-called "*interactive aerosol*" version reflects modifications to better represent the radiative impact of atmospheric dust and water-ice clouds [*Madeleine et al.*, 2011a]. In this new version, the dust layer depth is predicted rather than prescribed, as implemented by a "*semi − interactive*" dust transport scheme [*Madeleine*, 2011; *Madeleine et al.*, 2011b]. This scheme is called semi-interactive because the dust opacity profiles are predicted by the model, but scaled so that the total column opacity matches the dust opacity observed by TES. Note that in this paper, the model is constrained by the TES opacity observed during MY26, whereas the CRISM limb $O_2(^1\Delta_g)$ nightglow observations are acquired during MY29 and MY30. The dust particles serve as condensation nuclei for water-ice clouds, which are also radiatively active. The radiative effect of both dust and water-ice clouds depends on the size of the particles, and their radiative properties are constantly updated in the GCM as their spatial distribution and particle size evolve.

[24] In presenting the two distinct model cases, one might hope to find confirmation of the specific influences of cloud radiative forcing in the CRISM observations of $O_2(^1\Delta_g)$ polar nightglow. However it is also instructive to present comparisons for these two models in the context of model sensitivity to current uncertainties in Mars global circulation, particularly with respect to poleward meridional circulation at upper atmospheric levels.

4.2. Coincident MCS Profiles of Temperature (and Aerosols)

[25] Winter polar temperature profiles in the 40–60 km regions exhibit the same peaked structure as $O_2(^1\Delta_g)$ nightglow. In both cases, this is a direct consequence of polar convergent flow from upper levels associated with strong Hadley circulation in the fall-winter-spring atmosphere. Atmospheric temperatures also directly influence $O_2(^1\Delta_g)$ emission rates through the temperature dependent rate coefficient for $O_2(^1\Delta_g)$ production by three body recombination of atomic oxygen (equations (1) and (7)). In these respects, measurements of polar winter $O_2(^1\Delta_g)$ and temperature profiles illuminate comparable atmospheric processes. For the 2010 February–August period of CRISM limb observations, we have obtained MCS temperature and aerosol profile retrievals that are closest in time and space. While the MRO MCS and CRISM instruments do not obtain truly coincident limb views, the every-orbit operation of MCS allows fairly close coincidence in measurements between these experiments (typically within two hours of time, 2 degrees of latitude, and 15 degrees of longitude). The description of MCS profile retrievals may be found in *Kleinböhl et al.* [2009]. Key attributes include full global coverages at equatorial local times of 3 PM and 3 AM, 5 km vertical resolution over 0–80 km altitudes, and simultaneous temperature, dust and water ice profile solutions. Our use of the co-located MCS aerosol profiles is restricted to a determination that dust and ice aerosol extinction along the limb path of polar night $O_2(^1\Delta_g)$ emission is negligible. With respect to MCS temperature comparisons, we point out that MCS polar winter temperature profiles have already been compared to standard LMD GCM temperature profile simulations [*Forget et al.*, 1999]. These comparisons clearly demonstrate that the model does not predict accurate adiabatic heating profiles associated with polar downward convergence [*McCleese et al.*, 2008]. The combined CRISM $O_2(^1\Delta_g)$ and MCS temperature profile comparisons to LMD GCM simulations presented herein provide their first comparison to interactive aerosol GCM simulations of polar winter temperatures.

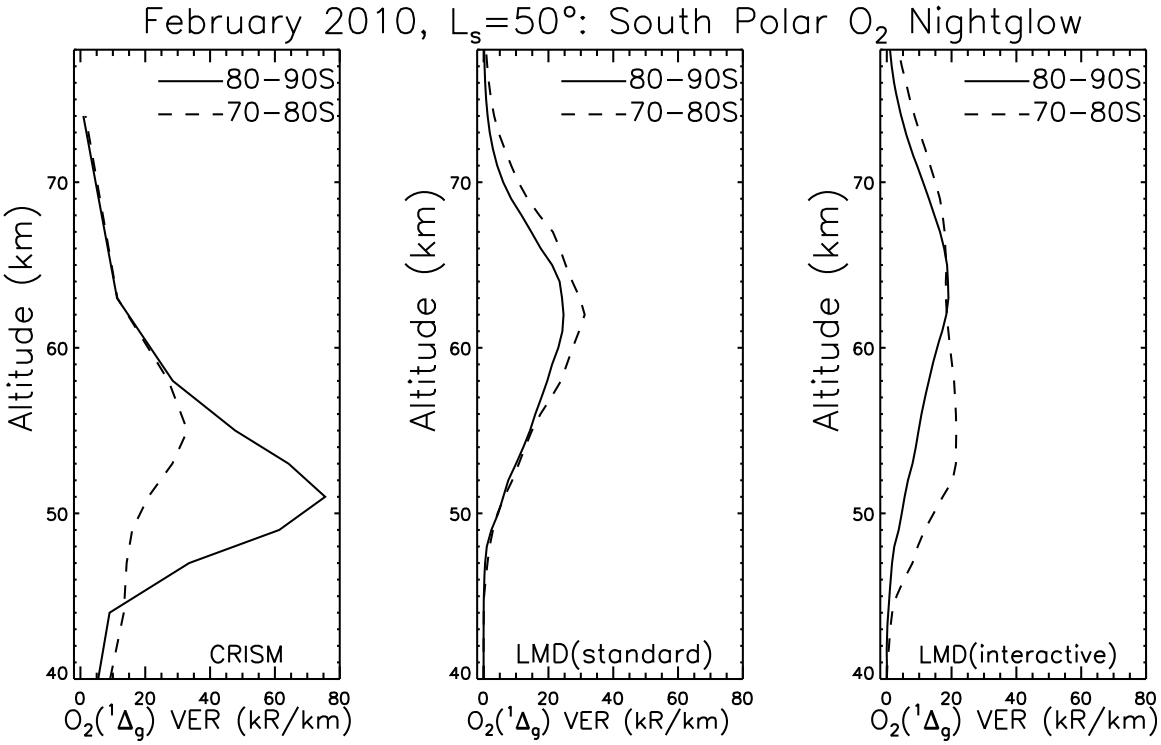

Figure 9. Averaged $O_2(^1\Delta_g)$ volume emission profiles (VER) from: (left) all CRISM retrievals on 10–11 February 2010 (L_S = 50°) for latitude bins of 70-80S (dashed lines) and 80-90S (solid lines); (middle) standard LMD GCM simulations co-located and contemporaneous with each CRISM measurement for the same latitude bins; (right) interactive aerosol LMD GCM simulations co-located and contemporaneous with each CRISM measurement for the same latitude bins in this late southern fall season.

4.3. CRISM/LMDGCM $O_2(^1\Delta_g)$ Comparisons

[26] We present CRISM profile retrievals of $O_2(^1\Delta_g)$ VER against two separate LMD GCM model simulations, employing standard and interactive aerosol models as described above. In all cases, the model and comparisons are co-located (latitude, longitude) and contemporaneous (same L_S and LT). We segregate the model-data by Mars season into three categories; southern winter, northern winter, and northern-southern equinoxes. Given the preponderance of 2010 observations, the most extensive portion of CRISM limb observations pertains to southern winter conditions (L_S = 50–137°). All of these southern winter periods correspond to CRISM limb observations that extend over the pole to obtain the highest latitudes (87S) and substantial diurnal coverage (where all hours still remain in polar darkness). The August 2010 period of multiple orbit coverage also enriches this data set relative to the others. The northern winter pole observations were obtained in 2009 (L_S = 301°) and 2011 (L_S = 265, 293°) with limited high latitude (lat ≤ 82N) and no AM local time coverages. The equinoctial periods consist of two 2010 periods (L_S = 166, 193°), for which nearly polar night conditions were obtained at high latitudes (>77NS) for both poles, with limited diurnal coverage. For these model-data comparisons of $O_2(^1\Delta_g)$ VER, we consider the average $O_2(^1\Delta_g)$ behaviors (vertical extent, peak amplitudes); and in the case of the L_S = 74–137° periods, their global (latitude, longitude) and temporal distributions (L_S and LT). We conclude this section with a consideration of the key parameters, atmospheric and atomic oxygen densities, which contribute to outstanding differences between observed and modeled $O_2(^1\Delta_g)$ polar night emission rates.

4.3.1. The 2010 Southern Winter

[27] In Figures 9–11, we compare the CRISM $O_2(^1\Delta_g)$ VER (Figures 9–11, left) to simulations for $O_2(^1\Delta_g)$ VER from the standard (Figures 9–11, middle) and interactive aerosol (Figures 9–11, right) LMD GCM models; for L_S periods of 50° (February 10–11, 2010), 74–96° (April 7, April 28–29, and May 26, 2010), and 137° (August 22–23, 2010), respectively. In each case, we show the averages of all observed and modeled $O_2(^1\Delta_g)$ VER profiles over the date intervals and within two latitude bins of 70S-80S (dashed lines) and 80S-90S (solid lines). The late southern spring season of February 2010 (L_S = 50°, Figure 9) presents the poorest agreement between observed and modeled $O_2(^1\Delta_g)$ VER profiles among all of the observed periods. Both model profiles present peak $O_2(^1\Delta_g)$ VER values above 60 km over 80-90S, versus the observed peak altitude of 51 km. The observations also indicate increasing $O_2(^1\Delta_g)$ VER toward the pole (*i.e.*, larger over 80-90S versus 70-80S), which is typical for all of the CRISM polar winter observations but most clearly displayed in this period. In contrast, the standard model presents fairly constant $O_2(^1\Delta_g)$ VER over 70-90S for this season, and the interactive aerosol model presents poleward decreasing $O_2(^1\Delta_g)$ emission at lower altitudes (45–55 km) for this season. The April, May 2010 period (L_S = 74–96° Figure 10) corresponds to southern winter solstice and provides perhaps the best agreement between

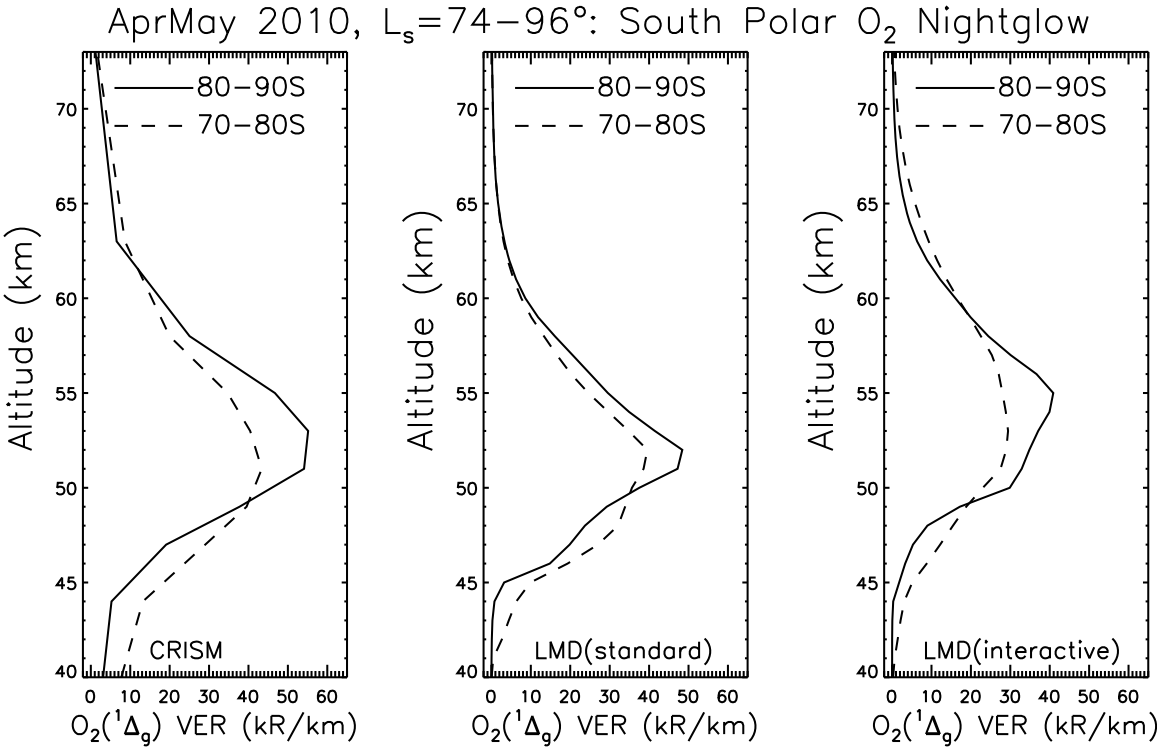

Figure 10. Averaged $O_2(^1\Delta_g)$ volume emission profiles (VER) from: (left) all CRISM retrievals on 7, 28–29 April and 26 May 2010 (L_S = 74–96°) for latitude bins of 70-80S (dashed lines) and 80-90S (solid lines); (middle) standard LMD GCM simulations co-located and contemporaneous with each CRISM measurement for the same latitude bins; (right) interactive aerosol LMD GCM simulations co-located and contemporaneous with each CRISM measurement for the same latitude bins in this southern winter solstice season.

observed and modeled $O_2(^1\Delta_g)$ VER profiles, in terms of altitude distribution and latitudinal gradient. The interactive aerosol model provides slightly improved observational agreement for the altitude of peak emission, relative to the standard model. Figure 11 presents $O_2(^1\Delta_g)$ VER profiles for late southern winter (August 2010, L_S = 137°), when both models present higher $O_2(^1\Delta_g)$ emission above 55 km than present in the CRISM observations. The interactive aerosol model provides somewhat better agreement with the observations, in terms of both vertical and latitudinal gradients of $O_2(^1\Delta_g)$ emission. Overall, these 2010 model-data comparisons for the average $O_2(^1\Delta_g)$ emission profile in southern polar night indicate modest improvements in agreement for interactive aerosol versus standard model simulations. Both models tend to bias $O_2(^1\Delta_g)$ emission to higher altitudes, relative to the observations, for late fall and late summer periods bounding the southern summer solstice. In contrast, the CRISM observations show minimal seasonal variation in $O_2(^1\Delta_g)$ vertical or latitudinal distributions over this same period. Hence, the observations indicate a more constant expression of winter polar Hadley circulation over an extended seasonal range (L_S = 50 = 137°) than exhibited by either model.

[28] Spatial/diurnal variations in the 2010 observations of southern polar $O_2(^1\Delta_g)$ nightglow provides somewhat stronger support to the interactive aerosol versus standard model simulations. The average profiles presented in Figures 9–11 correspond to a range of longitudes, local times (LT), and latitudes observed within each latitude bin at each observational period. Variations associated with these parameters are evident in the limb radiance profiles of Figure 6 for the April, May period of 2010 (L_S = 74–96°). A significant fraction of this variation corresponds to changes in LT of observation as the spacecraft passes over the south pole. Such behavior may indicate the influence of solar tides through modulation of the vertical transport of atomic oxygen at high latitudes. The LT coverage of CRISM observations itself is fairly limited and somewhat asymmetric about the pole, with irregularly sampled LT intervals of 2–10 PM and 1–5 AM. Given the sparse latitude/LT coverage of the February CRISM observations, we focus on the April–August period of southern winter (L_S = 74–137°). Figures 12 and 13 illustrate the latitude/LT variation of $O_2(^1\Delta_g)$ polar nightglow in southern winter for the April–May (L_S = 74–95°) and August (L_S = 137°) periods, respectively. Both figures present nadir column integrated values of $O_2(^1\Delta_g)$ VER from CRISM observations (Figures 12 and 13, top) and the LMD standard (Figures 12 and 13, middle), and interactive aerosol simulations (Figures 12 and 13, bottom). The plotted $O_2(^1\Delta_g)$ VER correspond to vertical columns integrated over the 46–75 km region, and so are roughly equivalent to nadir views of polar $O_2(^1\Delta_g)$ 1.27 μm

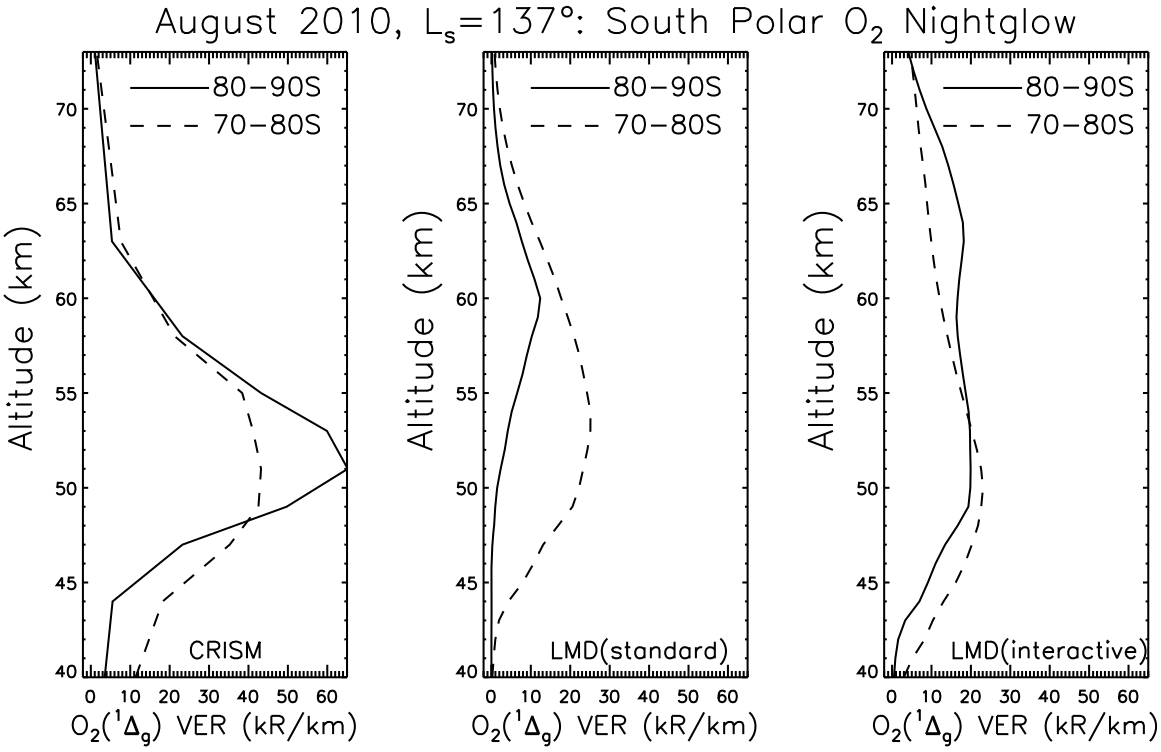

Figure 11. Averaged $O_2(^1\Delta_g)$ volume emission profiles (VER) from: (left) all CRISM retrievals on 22–23 August 2010 (L_S = 137°) for latitude bins of 70-80S (dashed lines) and 80-90S (solid lines); (middle) standard LMD GCM simulations co-located and contemporaneous with each CRISM measurement for the same latitude bins; and (right) interactive aerosol LMD GCM simulations co-located and contemporaneous with each CRISM measurement for the same latitude bins in this late southern winter season.

nightglow. They also provide a comparison of the total polar production of 1.27 μm nightglow associated with meridional transport of atomic oxygen, between the observations and the models. Over this period, the standard and interactive aerosol models produce 40% and 30% less 1.27 μm emission than the observations indicate, respectively. Observed latitudinal, LT gradients present in these southern winter polar $O_2(^1\Delta_g)$ VER appear more consistent with the interactive aerosol versus the standard LMD GCM gradients for the August period (Figure 13) in particular. The latitudinal gradient of 70–90S $O_2(^1\Delta_g)$ emission is relatively flat over the dayside (PM) hemisphere for the observations (Figure 13, top left) and interactive aerosol model (Figure 13, bottom), but distinctly decreasing toward the pole for the standard model (Figure 13, middle). On the nightside (AM) hemisphere, $O_2(^1\Delta_g)$ emission decreases away from the pole for the observations (Figure 13, top) and the interactive aerosol model (Figure 13, bottom), yet remains poleward decreasing in the standard model (Figure 13, middle). The standard model simulation of south polar 1.27 μm nightglow at L_S = 137° (Figure 13) effectively presents a minimum at the pole, surrounded by a maximum near 75S that extends over all (measured) local times. In contrast, the observations present relatively constant 1.27 μm emission up to the pole from the dayside (PM) hemisphere, whereupon it decreases into the nightside (AM) hemisphere. The interactive aerosol (Figure 13, middle) simulated $O_2(^1\Delta_g)$ emission behaves similarly, although the PM-to-AM gradient is considerable smaller than presented in the CRISM observations (10–20% versus 30–50%).

[29] The distinct latitudinal/LT gradients of polar 1.27 μm nightglow presented by the standard and interactive aerosol models suggest distinct polar transport morphologies as simulated by these models. The agreement between CRISM and interactive aerosol model latitudinal/LT distributions for the L_S = 137° period in particular would favor the polar circulation returned by the interactive aerosol model in this season. As demonstrated in a following section, the interactive aerosol model also provides improved agreement with respect to MCS temperature profiles at this time. The major cloud-radiative feature present in the global Mars atmosphere at this season is the aphelion cloud belt (ACB). These extensive water ice clouds tend to reinforce polar mesospheric convergence and associated adiabatic warming in the interactive aerosol model because they enhance the lower atmosphere source of thermal tides in the ACB, as found by *Hinson and Wilson* [2004]. Tropical clouds enhance the temperature diurnal cycle between the surface and 30 km, and thus thermal tides, primarily through their absorption of thermal radiation emitted by the surface. This induces strong warming during the day and cooling at night. Radiative effects of clouds on the thermal structure also affect the vertical transport of dust and that further contributes warming

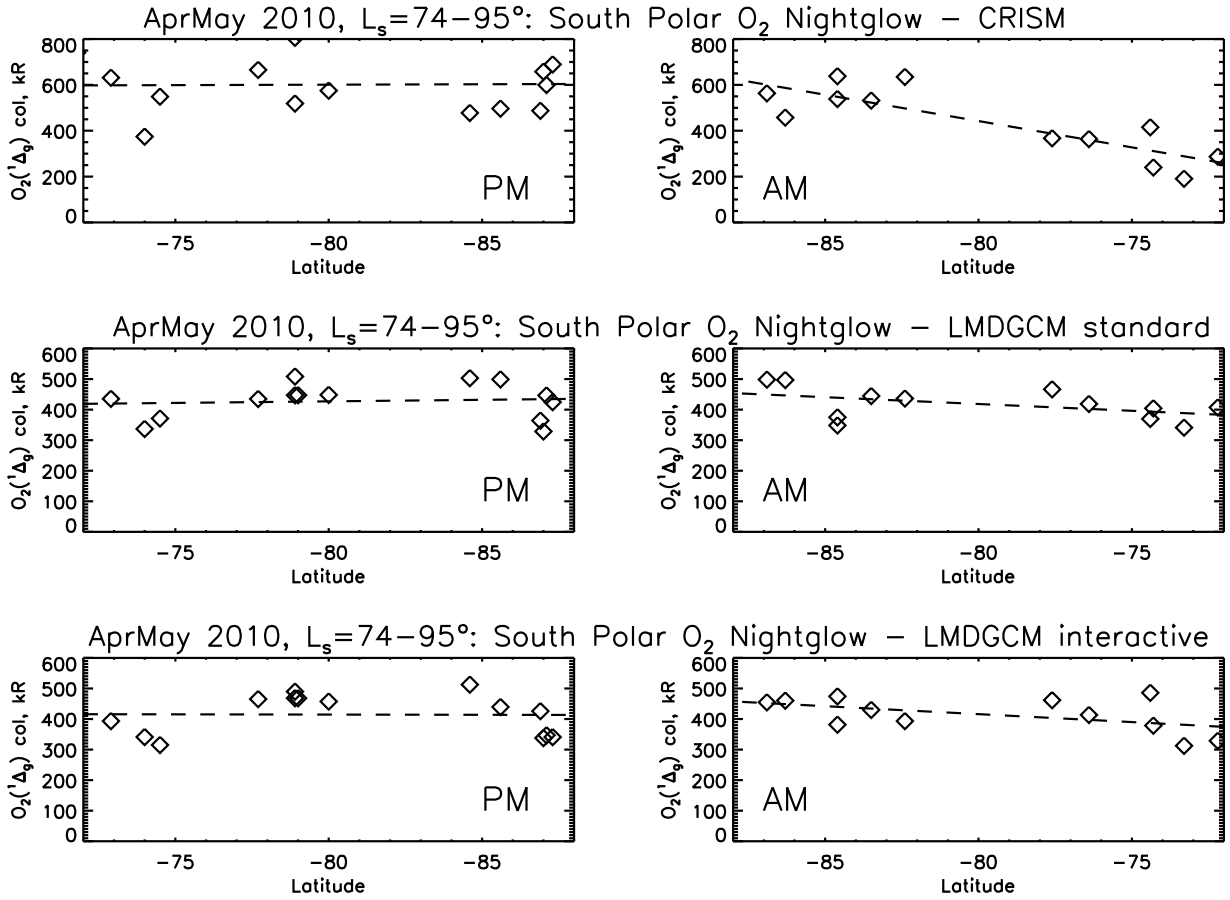

Figure 12. The latitudinal dependences of vertically integrated $O_2(^1\Delta_g)$ VER (~ nadir VER, see text) are presented for (left) PM and (right) AM local times, for (top) CRISM observations and (middle) standard and (bottom) interactive aerosol model simulations for the Apr-May period of CRISM observations (L_S = 74–95°). Dashed lines represent least squares linear fits to the latitudinal/diurnal trends. Both observations and model $O_2(^1\Delta_g)$ VER are fairly constant across PM latitudes to the pole, but decrease from the pole to lower AM latitudes in a fairly monotonic fashion.

of the northern summer tropical atmosphere between 10 and 40 km [*Madeleine*, 2011; *Madeleine et al.*, 2011b]. In terms of dynamics, the enhanced thermal tides tend to drag the mean flow toward their phase velocity (−240 m/sec). This affects the tropical zonal wind from above the clouds into the thermosphere. This, in turn, enhances the meridional circulation and thus the convergence of mass and its descent above the polar region. Hence, the seasonal, spatial and diurnal variations of southern winter $O_2(^1\Delta_g)$ polar nightglow (and temperatures) are affected by cloud radiative forcing, as the distinctions in standard and interactive model simulations demonstrate. Of course, we cannot argue that cloud radiative forcing is unambiguously identified in the CRISM polar night $O_2(^1\Delta_g)$ observations. Improved observational agreement is not consistently demonstrated by the interactive aerosol model among the all of the observed seasons, and both models seriously underpredict the time averaged $O_2(^1\Delta_g)$ polar nightglow.

4.3.2. The 2009, 2011 Northern Winter

[30] CRISM limb coverage of the northern winter pole is much more limited than that obtained for the southern winter pole in 2010. It consists of strictly PM local time observations obtained in July of 2009 (L_S = 301°) and March/April (L_S = 265°), May (L_S = 293°) of 2011. Northern polar winter highest latitude (80N-90N) measurements are further limited to only two 82N measurements obtained in May of 2011. Figure 14 presents the comparison of average northern polar winter profiles for latitude bins of 70N-80N (dashed lines) and 80N-90N (solid lines) against the standard (Figure 13, middle) and interactive aerosol (Figure 13, right) LMD GCM simulations for contemporaneous (L_S, LT), co-located (latitude, longitude) model averages. Both models and the CRISM observations indicate increasing $O_2(^1\Delta_g)$ with increasing latitude within the PM, LT ranges observed. However, this behavior is not well determined given the limited measurements above 80N at this time. In terms of northern versus southern polar winter comparisons (Figure 14 versus Figure 10), $O_2(^1\Delta_g)$ emission appears at lower elevations (relative to the surface aeroid) in the north versus the south by ~2–4 km in the observations and models. However, the northern relative to southern observed intensities of $O_2(^1\Delta_g)$ winter polar emission are observed as fairly

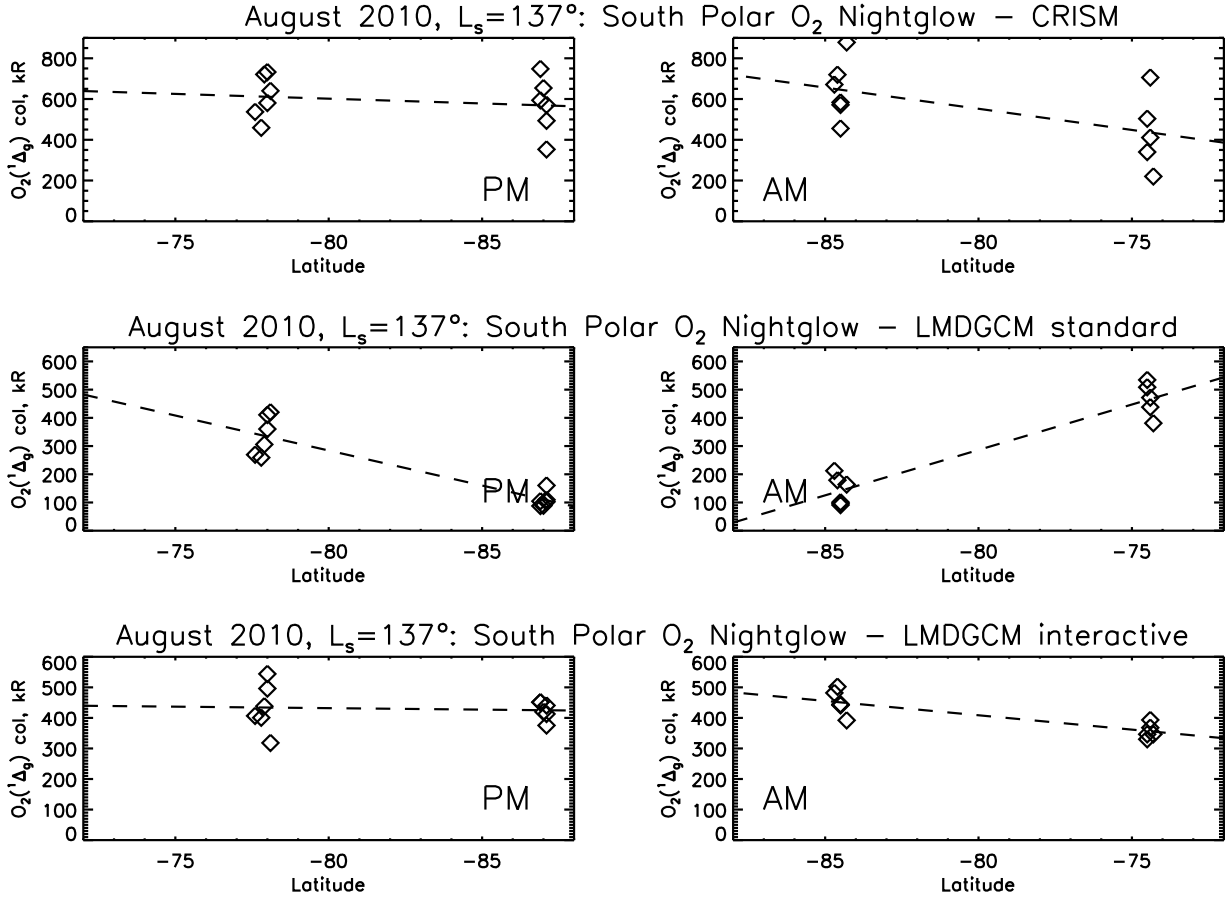

Figure 13. The latitudinal dependences of vertically integrated $O_2(^1\Delta_g)$ VER (~ nadir VER, see text) are presented for (left) PM and (right) AM local times, for (top) CRISM observations and (middle) standard and (bottom)interactive aerosol model simulations for the August period of CRISM observations (L_S = 137°). Dashed lines represent least squares linear fits to the latitudinal/diurnal trends. Similar to the Apr-May (L_S = 74–95°) behavior, the observations and interactive aerosol model $O_2(^1\Delta_g)$ VER are fairly constant across PM latitudes to the pole, but decrease from the pole to lower AM latitudes. In contrast, the standard model $O_2(^1\Delta_g)$ VER (Figure 13, middle) exhibit a distinctive, deep minimum in $O_2(^1\Delta_g)$ emission near the southern winter pole, coupled with diurnal symmetry.

comparable (within 10%). With respect to model-data comparisons, the observed northern solstice $O_2(^1\Delta_g)$ emission is significantly stronger than present in either the standard model (by 30%) or the interactive aerosol model (by 60%). Hence, the models underestimate $O_2(^1\Delta_g)$ polar nightglow by a significant margin (~40%) in both northern and southern polar winters.

[31] The distinction in $O_2(^1\Delta_g)$ integrated emission between the two models in this season are unlikely to be associated with radiative forcing by low latitude clouds such as the ACB, which are limited in extent by the warmer perihelion atmosphere [e.g., *Smith et al.*, 2001; *McCleese et al.*, 2010]. However, the northern polar hood is extensive and exerts considerable radiative forcing of the global circulation at this time. Furthermore, interactive aerosol simulations overproduce polar hood (and ACB) optical depths by factors-of-two, and so exaggerate its radiative effect in such models [*Madeleine et al.*, 2011a; *Haberle et al.*, 2011]. Hence, overestimation of poleward upper level circulation modification by north polar hood clouds may account in part for the difference between the two model $O_2(^1\Delta_g)$ emission rates.

4.3.3. The 2010 Northern and Southern Equinox

[32] Two sets of late 2010 CRISM limb observations, obtained on October 17 (L_S = 166°) and December 5–6 (L_S = 193), provide spring and fall polar conditions at the northern and southern poles. These are not strictly polar night conditions in that solar illumination is present at low elevation angles (~10°) for northern high latitudes (above 75N) in October and southern high latitudes (above 75S) in December. As indicated in Figures 15 and 16, averaged CRISM $O_2(^1\Delta_g)$ model VER profiles present lower altitude (below 45 km) increases that reflect $O_2(^1\Delta_g)$ production by ozone photolysis, for northern high latitudes in October and southern high latitudes in December. Nevertheless, distinctive high altitude $O_2(^1\Delta_g)$ emission is present in these seasons for both poles, associated with meridional transport and recombination of atomic oxygen. Each average profile presented in Figures 15 and 16 includes 6 to 7 limb

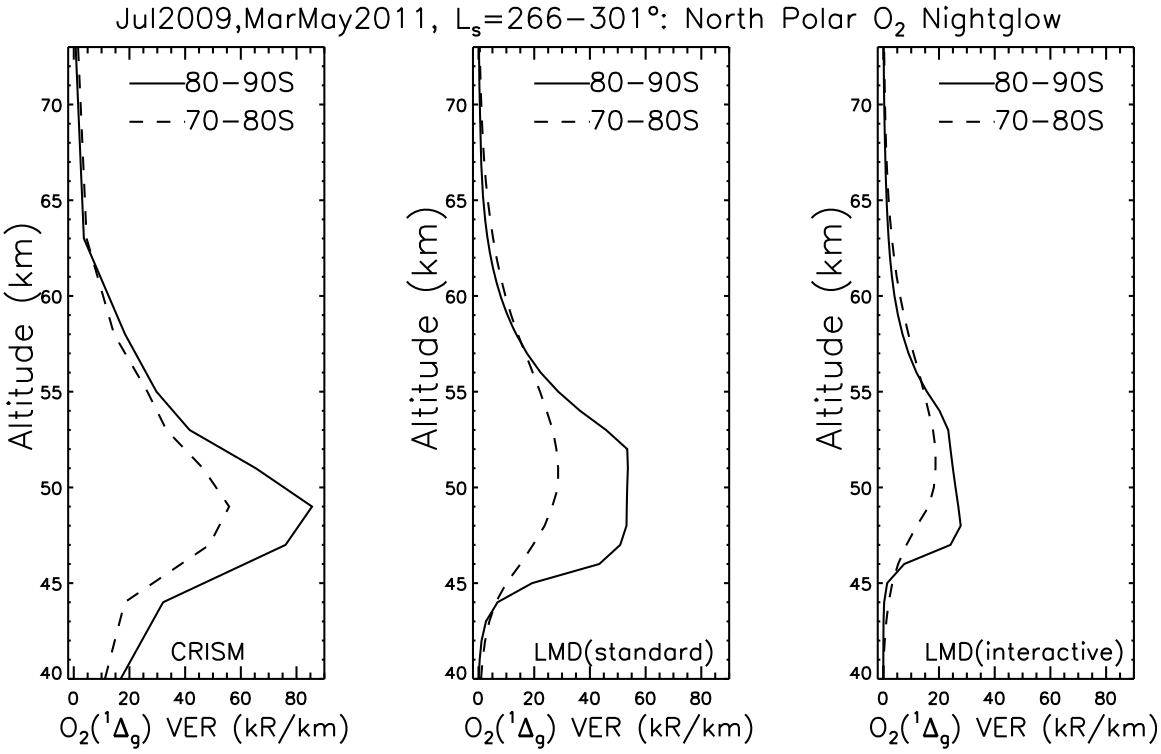

Figure 14. (left) Retrieved $O_2(^1\Delta_g)$ VER profiles are presented as averaged from July 10–11, 2009 (L_S = 301°); March 31–April 1, 2011 (L_S = 265°); and May 14–15, 2011 (L_S = 293°) CRISM limb observations. CRISM limb observations at 70-80N (dashed lines) and 80N-90N (solid lines) latitudes are compared to LMD GCM $O_2(^1\Delta_g)$ VER model profiles for (middle) standard and (right) interactive aerosol simulations averaged for the same L_S, LT, latitude, and longitude conditions.

observations that, for the limited numbers involved, do not show clear diurnal variation. Average column $O_2(^1\Delta_g)$ emission rates for these periods more closely approach the observed values for the standard (−20%) and interactive (+10%) models than for the solsticial periods.

[33] Notable symmetry is displayed between the observed north (solid lines) and south (dashed lines) polar $O_2(^1\Delta_g)$ profiles (Figures 15 and 16, left) in their variation between these L_S periods, which are similarly offset before and after northern fall/southern spring equinox (L_S = 180°). The peak altitude of $O_2(^1\Delta_g)$ emission varies by 5–10 km between the two polar regions, but in opposite sense between the periods. This behavior is not represented in the standard model simulation (Figures 15 and 16, middle), yet reasonably well represented in the interactive aerosol model. Differences between the two model $O_2(^1\Delta_g)$ emission profiles are most striking for north polar latitudes in both periods, and reflect large (factors-of-five) differences in simulated atomic oxygen densities, as discussed in the following section. Model differences in atmospheric density, as affected by differences in polar temperature profiles, are less than 30% for the same regions. As for the northern winter period, the primary distinction in cloud radiative forcing at this time regards waxing northern polar hood clouds of substantial optical depth that extend to the pole [*Benson et al.*, 2011]. By comparison, waning south polar hood clouds at this time are less optically thick and much more limited in latitudinal extent [*Benson et al.*, 2010].

4.3.4. Modeled and Observed Relationships Between $O_2(^1\Delta_g)$ Atmospheric Density, and Atomic Oxygen Density

[34] The disagreements between modeled and observed polar night $O_2(^1\Delta_g)$ emission are substantial in average magnitude (10–60%), vertical dependence, and seasonal character. Observed $O_2(^1\Delta_g)$ polar nightglow emission rates exhibit much less seasonal variation in integrated intensity and vertical distribution than simulated by either model. Here we consider two of the most prominent parameters that affect $O_2(^1\Delta_g)$ production, atmospheric density and oxygen density (equation (1)). Once again, we focus on the southern winter period of maximum number CRISM $O_2(^1\Delta_g)$ observations as well as coincident MCS density observations. Correlations with atmospheric temperature, employing coincident MCS temperature profiles, are presented in the following section. $O_2(^1\Delta_g)$ production rates are linearly proportional to atmospheric density through the three body recombination of atomic oxygen. In Figure 17, we compare the relationship between $O_2(^1\Delta_g)$ and atmospheric density as observed (Figure 17, left, CRISM/MCS) and modeled (Figure 17, right, for the interactive aerosol model). Both the model and the observations present a (noisy) anti-correlation, rather than correlation, between atmospheric density and $O_2(^1\Delta_g)$ polar nightglow, as averaged over the 50–55 km

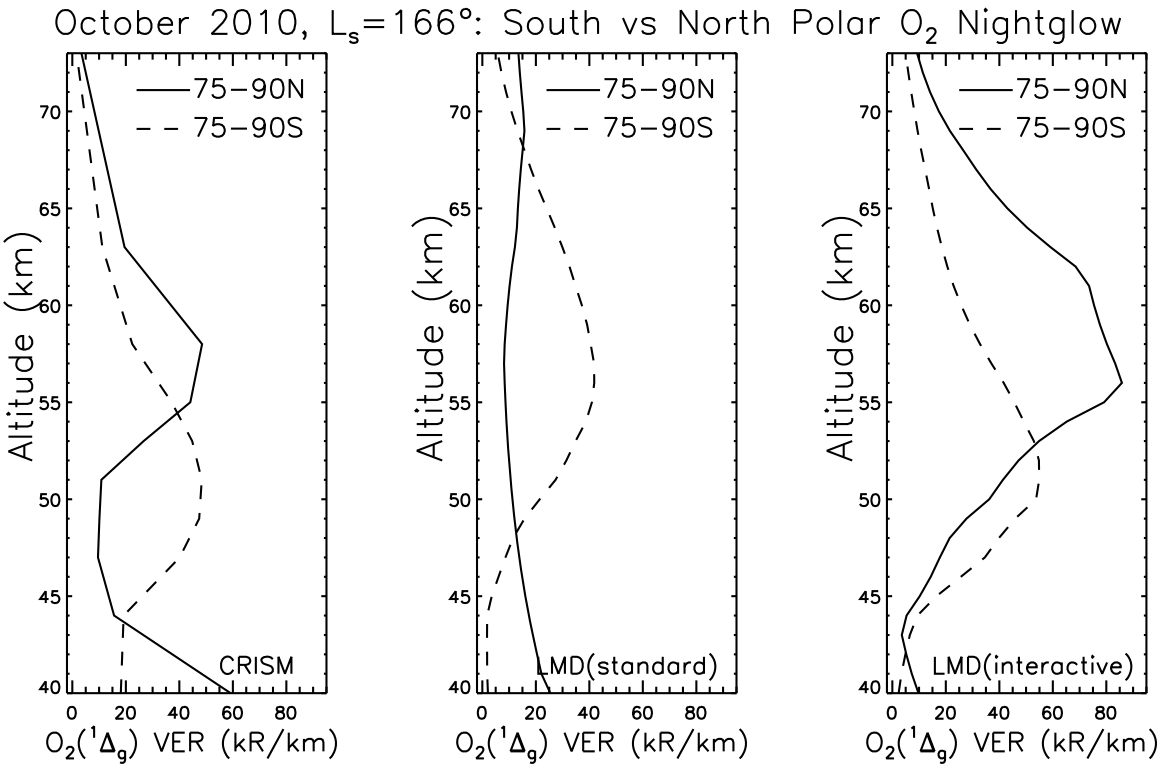

Figure 15. (left) Averaged $O_2(^1\Delta_g)$ VER profiles are presented from October 17, 2010 (L_S = 166°) CRISM limb observations at high southern (75S-90S, dashed lines) and high northern (75N-90N, solid lines), and compared to LMD GCM $O_2(^1\Delta_g)$ VER model profiles for (middle) standard and (right) interactive aerosol simulations averaged for the same L_S, LT, latitude, and longitude conditions in this pre northern fall equinox, southern spring equinox period.

altitude region of peak $O_2(^1\Delta_g)$ emission. This somewhat surprising result is due to a stronger, offsetting anti-correlation between atmospheric and atomic oxygen density in the polar winter upper atmosphere, as demonstrated in Figure 18. Here, atomic oxygen density is plotted versus atmospheric density (Figure 18, left) and $O_2(^1\Delta_g)$ VER (Figure 18, right), as simulated by the interactive aerosol model. We note that although $O_2(^1\Delta_g)$ atmospheric densities, and oxygen densities vary between the two model simulations, the general relationships presented in Figures 17 and 18 do not. Figure 18 (left) indicates that model atomic oxygen density is anti-correlated with model atmospheric density. This relationship, coupled with the quadratic dependence of $O_2(^1\Delta_g)$ emission with atomic oxygen density, explains the modeled (and observed) anti-correlation of polar $O_2(^1\Delta_g)$ nightglow with atmospheric density exhibited in Figure 17, as well as the modeled correlation of atomic oxygen density and $O_2(^1\Delta_g)$ nightglow presented in Figure 18 (right). That atmospheric density and atomic oxygen density are anti-correlated simply reflects the altitude-increasing (density-decreasing) profile of polar night atomic oxygen volume mixing ratio, as forced by atomic oxygen transport in the descending polar branch of the upper level circulation.

[35] Figures 17 and 18 effectively identify variable atomic oxygen density as the primary driver of spatial and temporal variations in $O_2(^1\Delta_g)$ polar nightglow. This variable atomic oxygen density in turn reflects variable poleward transport associated with the upper level meridional circulation. The distinctions between standard and interactive aerosol model simulations of $O_2(^1\Delta_g)$ polar nightglow reflect the influence of cloud radiative forcing on this upper level circulation. However, both models seriously underpredict $O_2(^1\Delta_g)$ nightglow emission as observed by CRISM over both winter poles, suggesting a more pervasive issue with GCM simulations of upper atmospheric polar conditions. A stronger, vertically deeper, and more extended-in-season poleward convergence appears to exist over the upper level polar winter atmosphere than presented in current MGCM simulations.

4.4. MCS/LMDGCM Temperature Comparisons

[36] Comparisons of MCS observed and LMD GCM modeled temperature profiles for the southern polar winter are provided in Figures 19 (L_S = 74–96°) and 20 (L_S = 137°). Both the model and MCS temperature profiles are selected as contemporaneous (L_S, LT) and co-located (latitude, longitude) with CRISM limb observations of $O_2(^1\Delta_g)$ in April 7, 27–28 and May 26 (Figure 19), and August 22–23 (Figure 20) of 2010. While we show that the detailed correlation of 40–60 km polar night temperatures and $O_2(^1\Delta_g)$ emission rates does not directly reflect the convergence of meridional circulation in the polar upper atmosphere (below), the general profile behaviors of winter polar temperatures and $O_2(^1\Delta_g)$ emission certainly do. Both exhibit distinctive peaks over

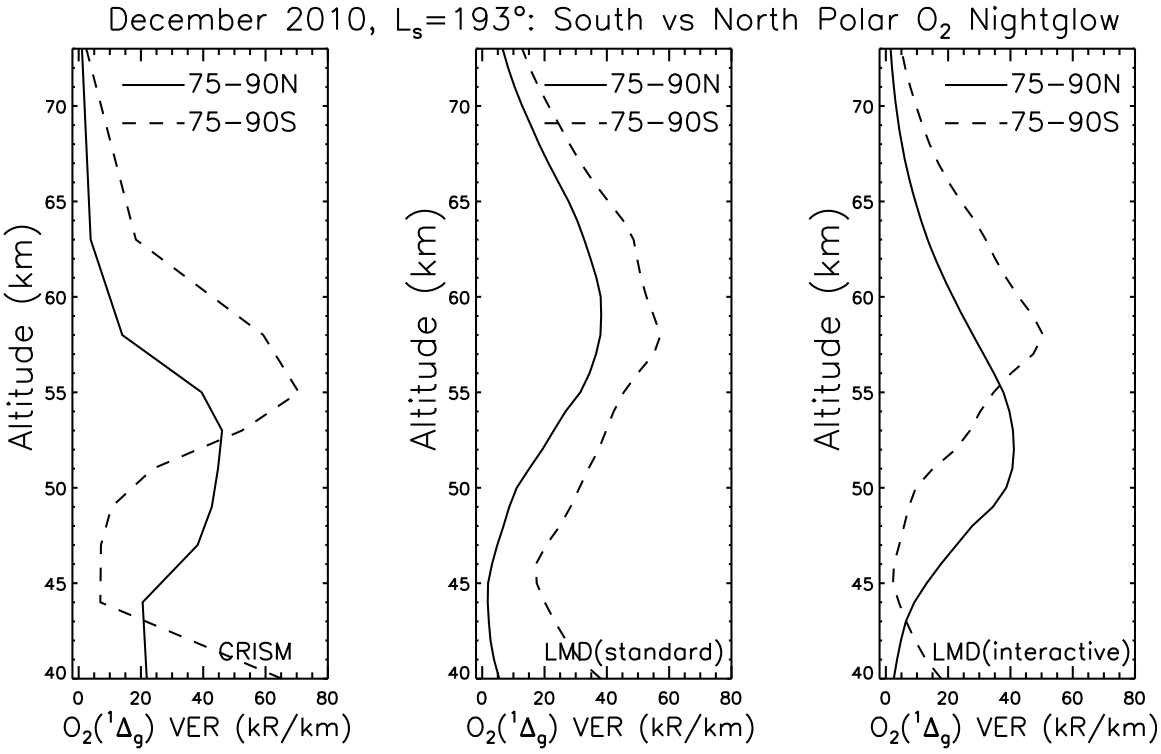

Figure 16. (left) Averaged $O_2(^1\Delta_g)$ VER profiles are presented from December 15–16, 2010 (L_S = 193°) CRISM limb observations at high southern (75S-90S, dashed lines) and high northern (75N-90N, solid lines) latitudes, and compared to LMD GCM $O_2(^1\Delta_g)$ VER model profiles for (middle) standard and (right) interactive aerosol simulations averaged for the same L_S, LT, latitude, and longitude conditions in this post northern fall equinox, southern spring equinox period.

40–60 km altitudes that correspond to the upper level poleward transport of atomic oxygen and adiabatic heating associated with the same polar convergent circulation. MGCM circulation models have not well reproduced the distribution of this polar heating, based upon initial LMD GCM comparisons with MCS polar winter temperature profile measurements [*McCleese et al.*, 2008]. The presented LMD CGM and CRISM southern polar winter $O_2(^1\Delta_g)$ distributions also indicate significant model-data discrepancies in standard model simulations that are somewhat mitigated by incorporation of active-aerosol processes in the LMD GCM simulations (notably Figures 13–15). Figures 19 and 20 show that, to varying degrees, incorporation of active-aerosol processes in the LMD GCM simulations also leads to general improvement in comparisons between MCS and LMD GCM southern winter polar temperature profiles. This improvement is not particularly notable in Figure 19 for model/data comparisons over April-May, 2010 (L_S = 74–96°), in which the interactive aerosol (dashed lines in Figure 19, bottom) simulated temperature profiles show modestly improved agreement with MCS profiles (solid lines) relative to standard model profiles (dashed lines in Figure 19, top) for the 70S-80S latitude range (Figure 19, left) in particular. More significant improvements in model/data comparisons are obtained for the August 2010 (L_S = 137°) period presented in Figure 20. In this case, the interactive aerosol simulated temperature profiles (dashed lines in Figure 20, bottom) compare significantly better with observed MCS profiles (solid lines) than the standard model simulated profiles (dashed lines in Figure 20, top) for both 70S-80S (Figure 20, left) and 80S-90S (Figure 20, right) latitude ranges. Hence, the incorporation of interactive aerosol processes in the LMD GCM improves model simulations of

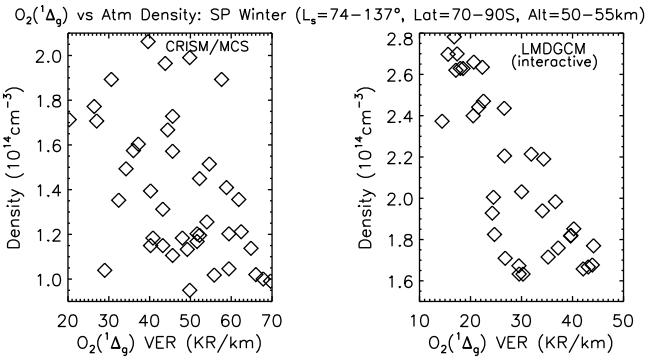

Figure 17. (left) Observed atmospheric densities (from MCS) versus $O_2(^1\Delta_g)$ emission rates (from CRISM), averaged over the 50–55 km altitude region from April, May, and August (L_S = 74–137°) periods of observation. (right) The same interactive aerosol model quantities, selected as coincident with observed locations (latitude, longitude) and times (L_S, LT). Similar anti-correlations between atmospheric density and $O_2(^1\Delta_g)$ emission rates are presented by the observations and model. This counterintuitive behavior is associated with anti-correlation between atmospheric density and oxygen density (Figure 18, see text).

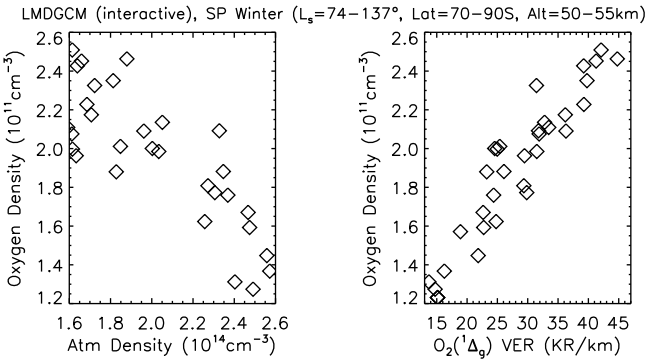

Figure 18. Oxygen densities from the interactive aerosol model, selected to be coincident with April, May, and August (L_S = 74–137°) CRISM observations, are averaged over the 50–55 km altitude region and plotted versus (left) averaged model atmospheric densities and (right) model $O_2(^1\Delta_g)$ emission rates. The anti-correlation of atmospheric density with oxygen density reflects the strong altitude-increasing gradient of atomic oxygen in the polar night upper atmosphere. The roughly linear dependence of $O_2(^1\Delta_g)$ emission with atomic oxygen density (Figure 18, right) reflects the quadratic dependence of $O_2(^1\Delta_g)$ production with atomic oxygen density (equation (1)) countered by the anti-correlation of atmospheric density (also in equation (1)) with atomic oxygen density (Figure 18, left).

southern polar winter temperatures and $O_2(^1\Delta_g)$ nightglow, although both models still depart significantly from the CRISM $O_2(^1\Delta_g)$ and MCS temperature profile measurements.

4.4.1. The Temperature Dependence of Winter Polar $O_2(^1\Delta_g)$ Emission

[37] A characteristic of $O_2(^1\Delta_g)$ nightglow in the Venus lower thermosphere is the correlation of 1.27 μm emission intensity with 10–20 K temperature increases over several thousand km regions, and the extreme temporal and spatial variabilities of this emission [*Crisp et al.*, 1996; *Bailey et al.*, 2008; *Ohtsuki et al.*, 2008; *Hueso et al.*, 2008]. Vertical downwelling rates associated with such Venus nightside regions of intense 1.27 μm emission (VER∼500 kR/km) and 20 K compressional temperature increases are estimated of order 20 cm/s [*Bailey et al.*, 2008]. LMD GCM vertical downwelling velocities within the Mars polar winter region of 1.27 μm emission are also of order 10′s cm/s. However, the pressure level of the Mars polar night peak limb emission (50 km, or ∼0.006 mbar) is typically ten times smaller than that of the Venus nightside lower thermospheric emission (∼0.06 mbar, assuming a 96 km altitude from *Drossart et al.* [2007], as are peak $O_2(^1\Delta_g)$ emission rates. Furthermore, the Mars polar winter $O_2(^1\Delta_g)$ emission is characterized by similarly reduced temporal and spatial variabilities. This particular difference apparently leads to very different correlations between local temperatures and

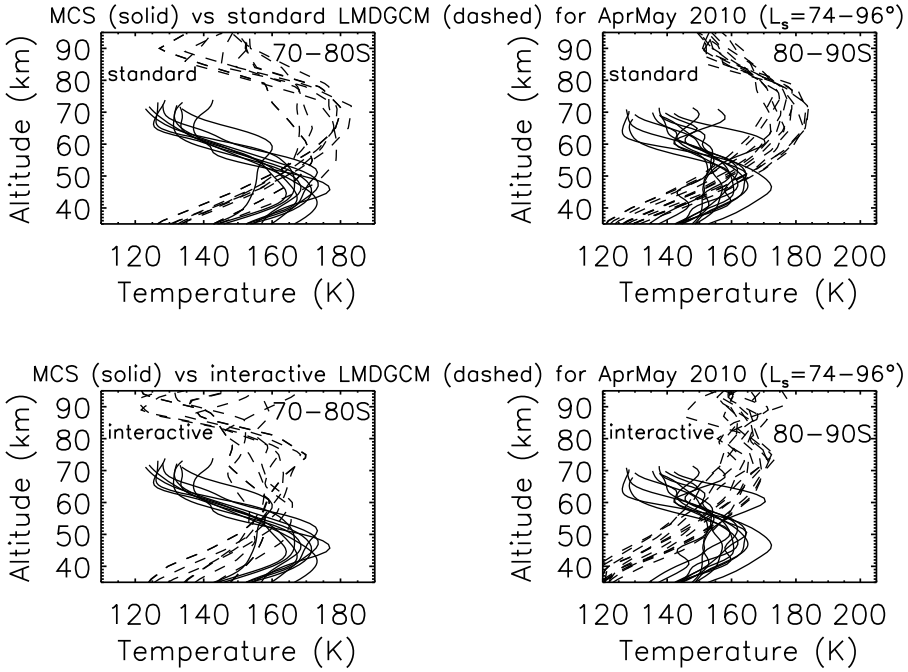

Figure 19. MCS observed (solid lines) and LMDGCM model (dashed lines) southern winter (L_S = 74–96°) polar temperature profiles are compared for (top) standard and (bottom) interactive aerosol simulations (see text). Model and observed values are binned for (left) 70S-80S and (right) 80S-90S latitude ranges. The model and observed profiles are contemporaneous (L_S, LT), co-located (latitude, longitude) with CRISM limb observations of $O_2(^1\Delta_g)$ obtained on April 7, 28–29 and May 26 of 2010. The interactive aerosol model profiles (Figure 19, bottom) provide moderately improved agreement with the MCS observed profiles over 70S-80S (Figure 19, left).

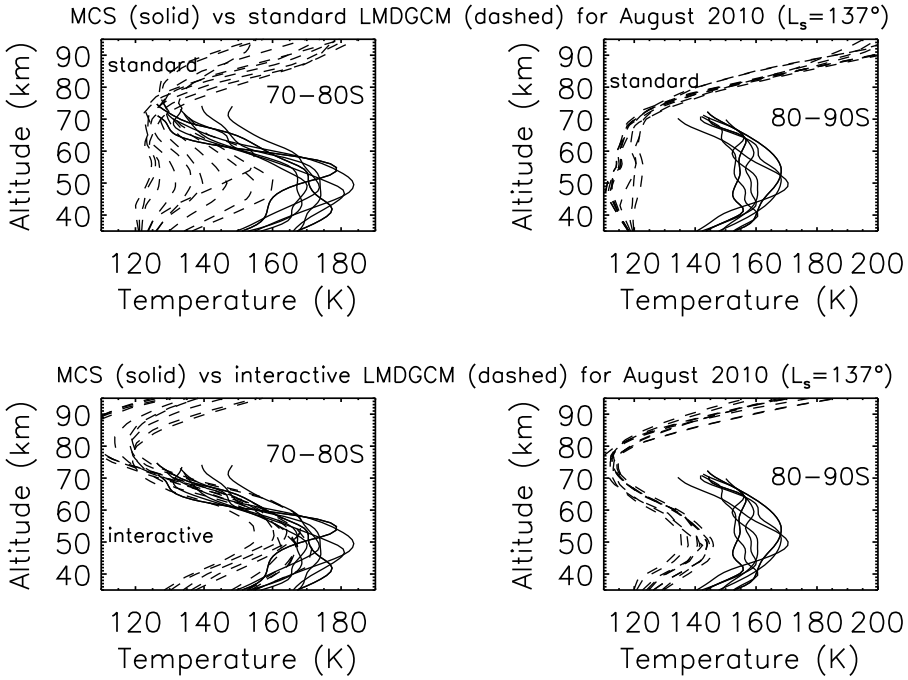

Figure 20. MCS observed (solid lines) and LMDGCM model (dashed lines) southern winter (L_S = 137°) polar temperature profiles are compared for (top) standard and (bottom) interactive aerosol simulations (see text). Model and observed values are binned for (left) 70S-80S and (right) 80S-90S latitude ranges. The model and observed profiles are contemporaneous (L_S, LT), co-located (latitude, longitude) with CRISM limb observations of $O_2(^1\Delta_g)$ obtained on August 22–23 of 2010. The interactive aerosol model profiles (Figure 20, bottom) provide significantly improved agreement with the MCS observed profiles over 70S-80S (Figure 20, left) and 80S-90S (Figure 20, right) latitude ranges.

1.27 μm VER in the Mars winter polar middle atmosphere versus the Venus nightside lower thermosphere.

[38] In Figure 21, we present plots of Mars southern polar winter (74-87S, L_S = 74–137°) 1.27 μm VER versus atmospheric temperature, from CRISM and MCS measurements (Figure 21, left) and from the LMD GCM simulation (Figure 21, right). Instead of the strong correlation in temperatures and $O_2(^1\Delta_g)$ emission observed for Venus, we see a noisy anti-correlation for Mars polar night temperatures and $O_2(^1\Delta_g)$ emission. This behavior is presented in both the CRISM/MCS observations and the LMD GCM model, to a very consistent degree (Figure 21 employs the interactive aerosol LMD calculations, but similar results apply from the standard model). The dashed lines plotted in Figure 21 represent least squares fits for exp(A/T) dependence between 1.27 μm VER and temperatures, with essentially identical derived coefficients, A, for the observations (380 $\pm$ 20) and model (430 $\pm$ 40). The exp(A/T) functional form reflects the temperature dependence of the rate coefficient for $O_2(^1\Delta_g)$ formation from atomic oxygen (equation (1)). The LMD GCM uses the temperature dependence employed by *Roble* [1995]; exp(480/T)) for the Mars $O_2(^1\Delta_g)$ simulations (see prior discussion in the LMD GCM description). The agreement between the observations and model demonstrated in Figure 9 provides some support for this assumption. The fitted observation and model values for this coefficient are perhaps slightly smaller (*i.e.*, 380–430 vs 480), but it does not appear that there is significant offsetting positive correlation between $O_2(^1\Delta_g)$ VER and temperatures. Hence, the correlation of such adiabatic heating with $O_2(^1\Delta_g)$ production is not clearly identified and so must be weak compared to conditions in the Venus nightside thermosphere.

[39] As a test of the model temperature-$O_2(^1\Delta_g)$ sensitivity, we have conducted LMD GCM simulations (interactive aerosol) employing the *Smith and Robertson* [2008] rate coefficient for reaction 1 in which the temperature sensitivity scales as exp(720/T). Employing the same model temperature-$O_2(^1\Delta_g)$ analysis above, we derive a value of 700 $\pm$ 50 for A. This is equivalent to the temperature sensitivity of the *Smith and Robertson* [2008] rate constant, further suggesting this rate constant dominates the model temperature-$O_2(^1\Delta_g)$ correlations. It also indicates that the temperature dependence of the *Smith and Robertson* [2008] rate constant leads to disagreement with the CRISM/MCS observations, whereas the temperature dependence of the adopted rate coefficient from *Roble* [1995] provides agreement.

5. Conclusions

[40] Vertically (46–75 km) integrated, latitudinally (70-90NS) averaged $O_2(^1\Delta_g)$ emission rates of 500–600 kR are retrieved from CRISM winter polar nightglow observations. The magnitude of LMD simulated polar nightglow is generally ~40% lower than these observed rates, for both northern and southern winter polar conditions. Simulated

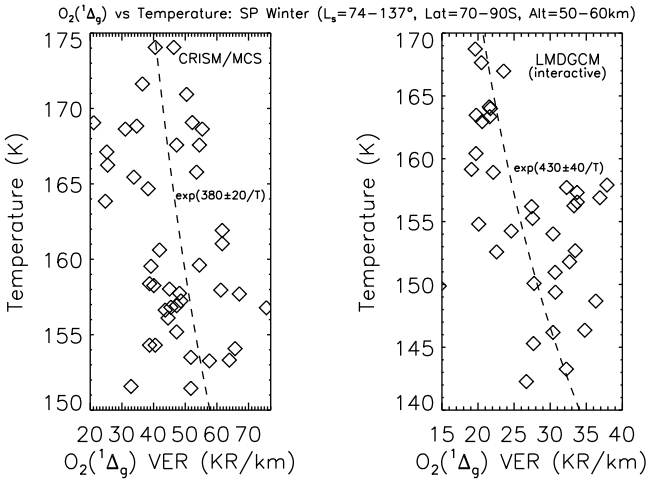

Figure 21. The correspondence between SP winter temperatures and $O_2(^1\Delta_g)$ 1.27 μm VER, as averaged over the 50–60 km altitude (aeroid) region for the CRISM locations (latitude = 70-90S, all longitudes) and times (L_S, LT) of limb observations from April-to-August, 2010 (L_S = 74–137°). (left) An observed anti-correlation between co-located CRISM $O_2(^1\Delta_g)$ and MCS temperature observations. (right) Very similar anti-correlation between LMD GCM $O_2(^1\Delta_g)$ and temperature simulations. The dashed lines in both panels indicate a functional fit to the presented $O_2(^1\Delta_g)$/temperature distributions, assuming the exp(A/T) dependence of the rate coefficient for winter polar $O_2(^1\Delta_g)$ formation (equation (1)). Very similar fits are found for the observations and model, where the derived coefficients are 380–430 K, as compared to the adopted model temperature coefficient of 480 K or a more recent laboratory determination of 720 K by *Smith and Robertson* [2008] (see text).

vertical profiles of winter polar $O_2(^1\Delta_g)$ emission also show much greater seasonal (L_S = 50–137, 266–301°) and vertical (46–75 km) variation than presented by observed $O_2(^1\Delta_g)$ profiles. Observed winter $O_2(^1\Delta_g)$ emission profiles exhibit more narrowly peaked emission regions centered at 50 ± 3 km for all of these periods, whereas simulated $O_2(^1\Delta_g)$ emission extends more broadly to altitudes above 60 km for the L_S = 50, 137° periods bounding winter solstice. Vertically integrated $O_2(^1\Delta_g)$ emission rates for two equinoctial periods (L_S = 166, 193°) exhibit better (10–20%) agreement between the observed and simulated polar regions (700–800 kR). Both equinoctial periods present distinctly offset $O_2(^1\Delta_g)$ emission peaks in the northern versus southern polar regions, behavior which is more clearly reproduced in the interactive aerosol versus standard LMD simulations. The LMD interactive aerosol model also better represents the latitudinal and diurnal $O_2(^1\Delta_g)$ variations presented by CRISM measurements as well as MCS polar temperature measurements at L_S = 137°. This southern winter period corresponds to the presence of the aphelion cloud belt, which leads to strong modulation on Mars thermal tides [e.g., *Hinson and Wilson*, 2004]. Such tidal influence further leads to enhanced zonal winds from the upper clouds levels (~40 km) into the thermosphere, for interactive aerosol LMD simulations [*Madeleine et al.*, 2011a, 2011b]. This in turn increases and diurnally modulates meridional circulation and mass convergence at southern winter latitudes, and thus mass convergence/descent over the pole. Northern polar hood clouds may play a related role in the distinctions between the equinoctial $O_2(^1\Delta_g)$ profiles simulated by the standard and interactive aerosol models.

[41] Model simulations and CRISM/MCS observations indicate strong anti-correlation between $O_2(^1\Delta_g)$ emission and atmospheric density at 50–55 km level of peak $O_2(^1\Delta_g)$ emission, counterintuitive to the relationship expected from the production reaction (1) for $O_2(^1\Delta_g)$. This behavior instead reflects the sharply increasing mixing ratio of atomic oxygen with altitude (*i.e.*, decreasing with density) over this region, associated with meridional transport and upper level convergence of atomic oxygen in the winter polar atmosphere. Both model simulations exhibit much stronger correlations between atomic oxygen density and $O_2(^1\Delta_g)$ emission. Hence, the transport efficiency of atomic oxygen plays the most important role in characterizing inadequate simulated versus observed winter polar $O_2(^1\Delta_g)$ emission rates. We also show that modeled and observed anti-correlations in $O_2(^1\Delta_g)$ emission rate and atmospheric temperature are in close agreement, and mimic the temperature dependence of the atomic oxygen recombination coefficient, specifically that given by *Roble* [1995]. This agreement does not hold when the *Smith and Robertson* [2008] rate coefficient temperature dependence is employed. In either case, there is no indication of correlated temperature and $O_2(^1\Delta_g)$ variations as exhibited in the Venus lower thermosphere [e.g., *Bailey et al.*, 2008].

[42] We have concluded that both the standard and the interactive LMD GCM models fail to provide sufficient transport of atomic oxygen to the winter polar regions of observed $O_2(^1\Delta_g)$ nightglow. Perhaps part of this failure is related to the outstanding disagreements in observed and simulated cloud optical depths associated with the interactive aerosol simulations [*Madeleine et al.*, 2011a; *Haberle et al.*, 2011]. It must be noted, however, that polar night upper atmospheric circulation, characterized here by the adiabatic warming and $O_2(^1\Delta_g)$ nightglow, is among the most sensitive phenomena in general circulation modeling. This sensitivity is particularly striking in model intercomparisons [e.g., *Mischna and Wilson*, 2008]. For instance, *Forget et al.* [1999] compared two models sharing the same physical parameterizations and only differing by the numerical methods to solve the atmospheric dynamic equations. The simulations were usually quite similar, except in the fall and winter polar night upper atmosphere where differences up to 30 K were found [see *Forget et al.*, 1999, Figure 8]. Similarly, any changes in poorly constrained processes, such as gravity wave drag, horizontal dissipation, convection and turbulence (which act near the surface, but influence the tides) have been found to significantly affect this part of the atmosphere, often without imparting significant changes elsewhere. The assumed upper atmosphere conditions can also play a role. For instance, in the version of the LMD GCM including a full thermosphere, the solar cycle variations of the extreme UV flux, which heats the thermosphere above 120 km, can change atmospheric temperatures by several Kelvins above 60 km in the polar night [*González-Galindo et al.*, 2009]. Polar night mesosphere observations of tracers such as $O_2(^1\Delta_g)$ and temperature thus provide unique constraints to test our

understanding of the Martian circulation and of planetary atmosphere dynamics in general.

[43] Last, extensive averaging of polar night CRISM limb spectra (over altitude, latitude, and time) reveal the 1.58 μm spectral emission of $O_2(^1\Delta_g)$ in the $\nu = 1$ vibrational state. The observed ratio of $O_2(^1\Delta_g)$ 1.27 μm to 1.58 μm emission is 80 $\pm$ 20, consistent with the same ratio observed in the Venus nightside lower thermosphere [*Piccioni et al.*, 2009].

[44] **Acknowledgments.** We are indebted to the excellent MRO and CRISM operations staff for the collection and processing of CRISM limb observations presented here. Grant support for this work was provided by the NASA MDAP Program (under NASA contract award number NNX10AL61G).

References

Altieri, F., L. Zasova, E. D'Aversa, G. Bellucci, F. G. Carrozzo, B. Gondet, and J.-P. Bibring (2009), O_2 1.27 μm emission maps as derived from OMEGA/MEx data, *Icarus*, *204*, 499–511.

Bailey, J., V. S. Meadows, S. Chamberlain, and D. Crisp (2008), The temperature of the Venus mesosphere from $O_2(a^1\Delta_g)$ airglow observations, *Icarus*, *187*, 247–259.

Benson, J. L., D. M. Kass, A. Kleinböhl, D. J. McCleese, J. T. Schofield, and F. W. Taylor (2010), Mars south polar hood as observed by the Mars Climate Sounder, *J. Geophys. Res.*, *115*, E12015, doi:10.1029/2009JE003554.

Benson, J. L., D. M. Kass, and A. Kleinböhl (2011), Mars north polar hood as observed by the Mars Climate Sounder, *J. Geophys. Res.*, *116*, E03008, doi:10:1029/2010JE003693.

Bertaux, J.-B., et al. (2005), Nightglow in the upper atmosphere of Mars and implications for atmospheric transport, *Science*, *307*, 567–569.

Bertaux, J.-L., B. Gondet, F. Lefèvre, J.-P. Bibring, and F. Montmessin (2012), First detection of O_2 1.27 μm nightglow emission at Mars with OMEGA/MEX and comparison with general circulation model predictions, *J. Geophys. Res.*, *117*, E00J04, doi:10.1029/2011JE003890.

Campbell, I. M., and C. N. Gray (1973), Rate constants for O(3P) recombination and association with N(4S), *Chem. Phys. Lett.*, *18*, 607–609.

Clancy, R. T., and H. Nair (1996), Annual (perihelion-aphelion) cycles in the photochemical behavior of the global Mars atmosphere, *J. Geophys. Res.*, *101*, 12,785–12,790.

Clancy, R. T., D. O. Muhleman, and G. L. Berge (1982), Microwave spectra of terrestrial mesospheric CO, *J. Geophys. Res.*, *87*, 5009–5014.

Clancy, R. T., B. J. Sandor, M. J. Wolff, P. R. Christensen, M. D. Smith, J. C. Pearl, B. J. Conrath, and R. J. Wilson (2000), An intercomparison of ground-based millimeter, MGS TES, and Viking atmospheric temperature measurements: Seasonal and interannual variability of temperatures and dust loading in the global Mars Atmosphere, *J. Geophys. Res.*, *105*, 9553–9571.

Colaprete, A., and O. B. Toon (2002), Carbon dioxide snow storms during the polar night on Mars, *J. Geophys. Res.*, *107*(E7), 5051, 10.1029/2001JE001758.

Conrath, B. J., et al. (1973), Atmospheric and surface properties of Mars obtained by infrared spectroscopy on Mariner 9, *J. Geophys. Res.*, *78*, 4267–4278.

Crisp, D., V. S. Meadows, B. Bézard, C. deBergh, J.-P. Mallaird, and F. P. Mills (1996), Ground-based near-infrared observations of the Venus nightside: 1.27-μm $O_2(^1\Delta)$ airglow from the upper atmosphere, *J. Geophys. Res.*, *101*, 4577–4594.

Drossart, P., et al. (2007), A dynamic upper atmosphere of Venus as revealed by VIRTIS on Venus Express, *Nature*, *450*, 642–645.

Fedorova, A., O. Korablev, S. Perrier, J.-L. Bertaux, F. Lefèvre, and A. Rodin (2006), Observation of O_2 1.27 μm dayglow by SPICAM IR: Seasonal distribution for the first Martian year of Mars Express, *J. Geophys. Res.*, *111*, E09S07, doi:10.1029/2006JE002694.

Forget, F., F. Frederic, R. Fournier, C. Hourdin, O. Talagrand, M. Collins, S. R. Lewis, P. L. Reid, and J.-P. Huot (1999), Improved general circulations models of the Martian atmosphere from the surface to above 80 km, *J. Geophys. Res.*, *104*, 24,155–24,176.

González-Galindo, F., F. Forget, M. A. López-Valverde, and M. Angelats i Coll (2009), A ground-to-exosphere Martian general circulation model: 2. The atmosphere during perihelion conditions—Thermospheric polar warming, *J. Geophys. Res.*, *114*, E08004, doi:10.1029/2008JE003277.

Haberle, R. M., et al. (1993), Mars atmospheric dynamics as simulated by the NASA/Ames general circulation model, *J. Geophys. Res.*, *98*, 3093–3124.

Haberle, R. M., F. Montmessin, M. A. Kahre, J. L. Hollingsworth, J. Schaeffer, M. Wolff, and R. J. Wilson (2011), Radiative effects of water ice clouds on the Martian seasonal water cycle, paper presented at The Fourth International Workshop of the Mars Atmosphere: Modeling and Observations, Paris, 8–11 February.

Hayne, P. O., D. A. Paige, J. T. Schofield, D. M. Kass, A. Kleinböhl, N. G. Heavens, and D. J. McCleese (2012), Carbon dioxide snow clouds on Mars: South polar winter observations by the Mars Climate Sounder, *J. Geophys. Res.*, doi:10.1029/2011JE004040, in press.

Hinson, D. P., and R. J. Wilson (2004), Temperature inversions, thermal tides, and water ice clouds in the Martian tropics, *J. Geophys. Res.*, *109*, E01002, doi:10.1029/2003JE002129.

Hueso, H., A. Sánchez-Lavega, G. Piccioni, P. Drossart, J. C. Gérard, I. Khatuntsev, L. Zasova, and A. Migliorini (2008), Morphology and dynamics of Venus oxygen airglow from Venus Express/Visible and Infrared Thermal Imaging Spectrometer observations, *J. Geophys. Res.*, *113*, E00B02, doi:10.1029/2008JE003081.

Hunten, D. M., F. E. Roach, and J. W. Chamberlain (1956), A photometric unit for the airglow and aurora, *J. Atmos. Terr. Phys.*, *8*, 345–346.

Kleinböhl, A., et al. (2009), Mars Climate Sounder limb profile retrieval of atmospheric temperature, pressure, and dust and water ice opacity, *J. Geophys. Res.*, *114*, E10006, doi:10.1029/2009JE003358.

Krasnopolsky, V. A. (2003), Mapping of Mars O_2 1.27 μm dayglow at four seasonal points, *Icarus*, *165*, 315–325.

Krasnopolsky, V. A. (2010a), Venus night airglow: Ground-based detection of OH, observations of O_2 emissions, and photochemical model, *Icarus*, *207*, 17–27.

Krasnopolsky, V. A. (2010b), Solar activity variations of thermospheric temperatures on Mars and a problem of CO in the lower atmosphere, *Icarus*, *207*, 638–647.

Krasnopolsky, V. A. (2011), Excitation of the oxygen nightglow on the terrestrial planets, *Planet. Space Sci.*, *59*, 754–766.

Lafferty, W. J., A. M. Solodov, C. L. Lugez, and G. T. Fraser (1998), Rotational line strengths and self-pressure broadening coefficients for the 1.27-μm $a^1\Delta_g - X^3\sum_g^-$, $\nu = 0$–0 Band of O_2, *Appl. Opt.*, *37*, 2264–2270.

Langevin, Y., J.-P. Bibring, F. Montmessin, F. Forget, M. Vincendon, S. Douté, F. Poulet, and B. Gondet (2007), Observations of the south seasonal cap of Mars during recession in 2000–2006 by the OMEGA visible/near-infrared imaging spectrometer on board Mars Express, *J. Geophys. Res.*, *112*, E08S12, doi:10.1029/2006JE002841.

Lefèvre, F., S. Lebonnois, F. Montmessin, and F. Forget (2004), Three-dimensional modeling of ozone on Mars, *J. Geophys. Res.*, *109*, E07004, doi:10.1029/2004JE002268.

Lefèvre, F., J.-L. Bertaux, R. T. Clancy, T. Encrenaz, K. Fast, F. Forget, S. Lebonnois, F. Montmessin, and S. Perrier (2008), Heterogeneous chemistry in the atmosphere of Mars, *Nature*, *454*, 971–975.

Madeleine, J.-B. (2011), *Nuages et poussières de l'atmosphère martienne: Télédétection, modélisation des rétroactions climatiques et application aux paléoclimats*., PhD thesis, Univ. Pierre et Marie Curie, Paris.

Madeleine, J.-B., F. Forget, and E. Millour (2011a), Modeling radiatively active water ice clouds: Impact on the thermal structure and water cycle, paper presented at The Fourth International Workshop on the Mars Atmosphere: Modeling and Observations, Paris, France, 8–11 February.

Madeleine, J.-B., F. Forget, E. Millour, L. Montabone, and M. J. Wolff (2011b), Revisiting the radiative impact of dust on Mars using the LMD Global Climate Model, *J. Geophys. Res.*, *116*, E11010, doi:10.1029/2011JE003855.

McCleese, D. J., et al. (2008), Intense polar temperature inversion in the middle atmosphere of Mars, *Nat. Geosci.*, *1*, 745–749, doi:10.1038/ngeo332.

McCleese, D. J., et al. (2010), Structure and dynamics of the Martian lower and middle atmosphere as observed by the Mars Climate Sounder: Seasonal variations in zonal mean temperature, dust, and water ice aerosols, *J. Geophys. Res.*, *115*, E12016, doi:10.1029/2010JE003677.

Mischna, M. A., and R. J. Wilson (2008), The Mars general circulation model intercomparison study, paper presented at the The Third International Workshop on the Mars Atmosphere: Modeling and Observations, Williamsburg, Va., 10–13 November.

Montmessin, F., F. Lefèvre, J.-L. Bertaux, and B. Gondet (2011), Transport-driven formation of an ozone layer at the Mars winter poles, paper presented at The Fourth International Workshop on the Mars Atmosphere: Modeling and Observations, Paris, 8–11 February.

Murchie, S. L., et al. (2007), Compact Reconnaissance Imaging Spectrometer for Mars (CRISM) on Mars Reconnaissance Orbiter (MRO), *J. Geophys. Res.*, *112*, E05S03, doi:10.1029/2006JE002682.

Murchie, S. L., et al. (2009), Compact Reconnaissance Imaging Spectrometer for Mars investigation and data set from the mars Reconnaissance Orbiter' primary science phase, *J. Geophys. Res.*, *114*, E00D07, doi:10.1029/2009JE003344.

Nair, H., M. Allen, A. D. Anbar, and Y. L. Yung (1994), A photochemical model of the Martian atmosphere, *Icarus*, *111*, 124–150.

Neumann, G. A., D. E. Smith, and M. T. Zuber (2003), Two years of clouds detected by the Mars Orbiter Laser Altimeter, *J. Geophys. Res.*, *108*(E4), 5023, doi:10.1029/2002JE001849.

Novak, R. E., M. J. Mumma, M. A. DiSanti, N. Dello Russo, and K. Magee-Sauer (2002), Mapping of ozone and water in the atmosphere of Mars near the 1997 aphelion, *Icarus*, *158*, 14–23.

Noxon, J. F., W. A. Traub, N. P. Carleton, and P. Connes (1976), Detection of O_2 dayglow emission from Mars and the Martian ozone abundance, *Astrophys. J.*, *207*, 1025–1035.

Ohtsuki, S., N. Iwagami, H. Sagawa, M. Ueno, Y. Kasaba, T. Imamura, K. Yanagisawa, and E. Nishihara (2008), Distributions of the 1.27-μm O_2 airglow and rotational structure, *Planet. Space Sci.*, *56*, 1391–1398.

Piccioni, G., L. Zasova, A. Migliorini, P. Drossart, A. Shakun, A. G. Muñoz, F. P. Mills, and A. Cardesin-Moinelo (2009), Near-IR oxygen nightglow observed by VIRTIS in the Venus upper atmosphere, *J. Geophys. Res.*, *114*, E00B38, doi:10.1029/2008JE003133.

Roble, R. G. (1995), Energetics of the mesosphere and thermosphere, in *The Upper Mesosphere and Lower Thermosphere: A Review of Experiment and Theory*, *Geophys. Monogr. Ser.*, vol. 87, edited by R. M. Johnson and T. L. Killen, pp. 1–21, AGU, Washington, D. C.

Rothman, L. S., et al. (2009), The HITRAN 2008 molecular spectroscopic database, *J. Quant. Spectrosc. Radiative Transfer*, *110*, 533–572.

Smith, G. P., and R. Robertson (2008), Temperature dependence of oxygen atom recombination in nitrogen after ozone photolysis, *Chem. Phys. Lett.*, *458*, 6–10.

Smith, M. D., J. C. Pearl, B. J. Conrath, and P. R. Christensen (2001), Thermal Emission Spectrometer results: Mars atmospheric thermal structure and aerosol distribution, *J. Geophys. Res.*, *106*, 23,929–23,945.

Smith, M. D., M. J. Wolff, R. T. Clancy, and S. L. Murchie (2009), Compact Reconnaissance Imaging Spectrometer observations of water vapor and carbon monoxide, *J. Geophys. Res.*, *114*, E00D03, doi:10.1029/2008JE003288.

Sprague, A. L., W. V. Boynton, K. E. Kerry, D. M. Janes, N. J. Kelly, M. K. Crombie, S. M. Nelli, J. R. Murphy, R. C. Reedy, and A. E. Metzger (2007), Mars atmospheric argon: Tracer for understanding Martian atmospheric circulation and dynamics, *J. Geophys. Res.*, *112*, E03S02, doi:10.1029/2005JE002597.

Wolff, M. J., M. D. Smith, R. T. Clancy, R. Arvidson, M. Kahre, F. Seelos IV, S. Murchie, and H. Savijärvi (2009), Wavelength dependence of dust aerosol single scattering albedo as observed by the Compact Reconnaissance Imaging Spectrometer, *J. Geophys. Res.*, *114*, E00D04, doi:10.1029/2009JE003350.